

The manuscript describes the set-up, attitude control, and exemplary measurements of two vertical pointing radars onboard RV MS Merian during Eurec4a. Main focus of this data paper is the compensation of the ship motion in situations where the active stabilization platform was properly working and different treatment of data in situations where the platform got stuck in arbitrary orientations.

The manuscript is consistent and well written and certainly deserves publication as data paper. There are only minor modifications required. I like the lessons learned section, I hope that this will be considered in future campaigns.

We thank the reviewer for the attentive and constructive review of the publication.

Some general comments:

Obviously, the authors did develop the methods behind the ship motion correction by themselves, without borrowing from the airborne radar community (e.g. Bange, J. et al., 2013: Measurement of aircraft state and thermodynamic and dynamic variable, in: Airborne Measurements for Environmental Research: Methods and Instruments, edited by: Wendisch, M. and Brenguier, J-L., <https://doi.org/10.1002/9783527653218.ch2>). The methods are the same and there is an agreement between the two worlds (air – sea).

Based on the reviewer's suggestions, we expanded the literature review on the topic, exploring the Bange et al 2013 text suggested (<https://onlinelibrary.wiley.com/doi/10.1002/9783527653218.ch2>) which is also part of the book "Airborne Measurements for Environmental Research: Methods and Instruments" by M. Wendisch and J-L. Brenguier (<https://onlinelibrary.wiley.com/doi/book/10.1002/9783527653218>) with particular interest in the chapter 9 on LIDAR and RADAR observations. However, we did not find specific mentions on corrections for mispointing on a moving platform. Therefore, we decided to add a general sentence as follows: "Similar methods have been derived for airplane based measurements with Doppler measurements see e.g. Bange et al, 2013".

For the W-band radar you do not mention anything about attenuation (gaseous, liquid) which certainly has to be considered, you call it just reflectivity (factor). Whereas for the MRR you talk about attenuated equivalent reflectivity (factor). This should be consistent. Otherwise one might assume that data from W-band radar are corrected for gaseous and liquid attenuation as well as for Mie effects. Reflectivity factor z implies Rayleigh approximation. However, since both systems are mm-wave systems you better write about effective reflectivity factor. This implies that Mie scattering effects have to be considered in the interpretation of reflectivity factor.

Thank you for this comment. The reflectivity provided by the postprocessing of the Wband radar(94 GHz, so λ is 3.19 mm) data is the equivalent reflectivity factor, i.e. the reflectivity calculated from the measured returned power assuming that the target is composed of liquid water droplets whose diameter is less than one tenth of the radar wavelength (droplets are treated as Rayleigh scatterers). When drops are larger than 3 mm, which is often the case in the data we collected, this approximation is not true and the equivalent reflectivity factor differs from the reflectivity factor. On top of that, while the RPG manual In (https://www.radiometer-physics.de/downloadftp/pub/PDF/Cloud%20Radar/RPG-FMCW-Instrument_Manual.pdf) details the gas loss correction, liquid attenuation affects the estimation of the equivalent reflectivity factor provided. All Wband radars as the one deployed on the ship (from RPG) provide in their data the equivalent reflectivity factor without corrections for liquid attenuation and Mie scattering because always Rayleigh approach is applied and we published the data following this line of conduct. Subsequent scientific publication planned on precipitation will focus on this aspect and provide the correction for Mie and liquid absorption for Wband radar data and compare them properly (on same resolution in time and space) with MRR data.

For the MRR data, the postprocessing algorithm calculates the equivalent radar reflectivity taking into account the attenuation due to liquid water contained in raindrops as well as the equivalent reflectivity non attenuated. For the MRR case, it is more difficult to get out of the Rayleigh approximation for the data collected, due to the different wavelength, but by definition, the equivalent reflectivity factor is assuming Rayleigh approach.

The plots show the equivalent reflectivity without any correction applied, so they are coherent with respect to the displayed quantity. We clarified better the differences between the datasets regarding the Rayleigh hypothesis.

I think the labels/numbers in the figures are too small, but I leave this to the technical editor.

We also wait for the technical editor's opinion on this. Thank you for noticing this aspect.

Reply to minor comments:

Line 14: I think DOI's have to be given in the abstract, but this is a task for the technical editor

We also do not know what is the best practice here. We wait for technical editor comments.

Line 22: What does OA stand for?

OA stands for ocean-atmosphere and is an acronym that represents the ocean-atmosphere research component that was part of the EUREC4A campaign (<https://eurec4a.eu/overview/eurec4a-oa/>). We included it because the RV Maria S. Merian was deeply involved in the operations regarding the investigation of sea-air interactions and the mesoscale eddies impact on the boundary layer. We included in the text a description of the OA and the link.

Line 69: Section instead of Session

Thank you for the comment, corrected.

Line 78: can you give here some numbers about the temporal drift

We added a estimation of the drift time. However, the drift is variable in time. We modified the sentence as follows: " Despite this effort, the time stamp synchronization suffered from a drift of the clocks with respect to the Global Positioning System (GPS) time of the ships inertial system variable between 1 and 4 s that we had to consider in the correction of the data for ship motions. "

Line 127: Why longitude and latitude with the same temporal resolution as the radar data are not copied to the radar dataset?

The latitude and longitude data come from the ship because they haven't been recorded by the radar. The lat and lon data have been resampled on the radar time resolution in the daily file version which is published online. Daily files are supposed to be used from the largest amount of users because they are ncdf files in a standardized format, easy to read and contain all the meteorological variables of interest.

Lat and lon are not included in the hourly radar files because such files contain only the radar-specific information, on top of the radar variables, and are of interest for specific radar applications only.

Lines 170 - 175: can you also give the temporal resolution of the MRU?

We added that the temporal resolution of the MRU is 1 s, thank you for the comment. The sentence reads now as follows: "All rotation angles are measured by the Motion Reference Unit (MRU) unit on the ship with a time resolution of 1 s."

Lines 179 - 184: this should go to section 2.3

Thank you for the comment: the sentence was somehow doubled, so we added some parts in section 2.3 and we left here only the sentence related to the figure 4. Please check the resulting text in the diff_versions.pdf file attached.

Figure 5 is hardly readable, the sketch of MS Merian is 2D, whereas the vectors are 3D; this figure should be improved considerable

We thank the reviewer for these comments. The readability has been improved by enlarging the fonts. We modified the image by splitting it in two parts. On one side one image of the RV, on the other we added the 3D reference system.

Lines 206 + 207: "whereas w_{heave} ... gates" is repeated from above

Thank you for the comment. We stated it again because we wanted to clarify why by averaging over height the w_{heave} does not change. However, we removed the second sentence since your suggestion indicates that it is redundant.

Lines 224 - 230: confusing, e_x, e_y, e_z is first ship relative and later horizon relative, maybe you could use different notations for the two reference systems

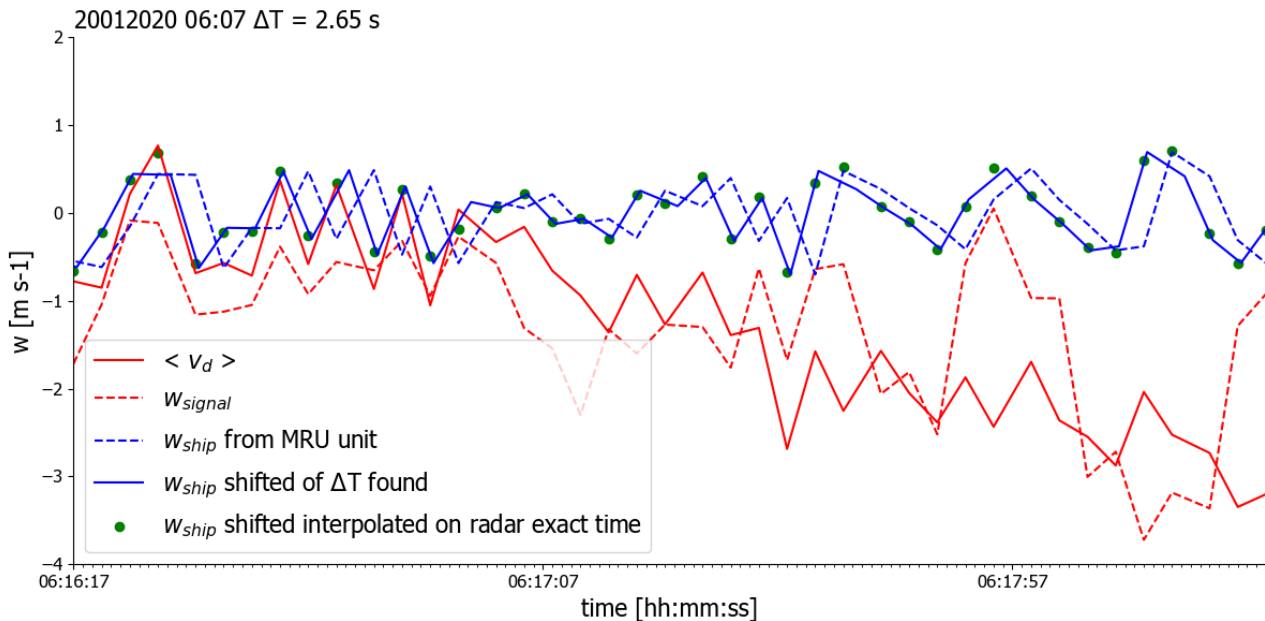
We thank the reviewer for the comment. Since the ship reference system and the horizontal reference system differ only because of the z direction, we preferred to keep the same notation, and just specify the direction. We went through the text and found an inaccuracy in the reference to the reference system. We corrected that and we hope that now the text can be less confusing.

Line 226: appendix C or equation C4

Corrected, thank you!

Figure 6: faint lines are hard to read, you could also use dashed lines instead

Please find here the new version of the plot:



This image has been substituted to the old Figure 6

Line 239: horizontal or ship relative coordination system? These are different reference systems

Horizontal reference system here. E_p is expressed with respect to the horizontal coordinate system

Line 262: v_{trans} would be more memorable for the translation velocity than v_{trasl}

We changed the naming

Line 264? - rotation vector: what is about bending and twisting of the ship body (I remember a video you showed once at a workshop)

Unfortunately there is no way to our knowledge to measure bending and twisting of the ship body itself. Also, We assumed that such deformations could be neglected because we did not experience rough sea conditions.

Figure 7: maybe panels a), b), c), e), f), g) could be larger, and d) and h) could be smaller (or omitted)

The figure was modified, thanks for the comment. We also extended the color bar range, to avoid the saturation for high $V_{doppler}$ values (see comment below)

Line 296: Figure 7 e)-g)

corrected thank you

Line 298: the high fall velocities in the second half of the plot and persistent through all heights seem unrealistic, can you comment on this?

In this plot, we chose to represent a precipitating shallow cumulus cloud not extending above the inversion and a deeper cumulus with top above 3000 m, to represent the variability in precipitation that we observed during the campaign. The high fall velocities observed are generated by the deeper cloud core, and the unrealistic effect mostly come from the fact that we used the same color bar for Doppler velocities even if the observed velocities span different ranges. A modified version of the plot has been prepared to avoid the saturation in the v_d more negative values.

Line 311: signal to noise "ratio" corrected

Line 313: Table 2 gives 7.5 to 34 m resolution. For the horizontal resolution also beamwidth has to be considered

Values presented in the table are provided by the manufacturer and refer to range vertical resolution.

We included in the table that is vertical resolution.

Line 321: numbering Fig. A1 is confusing. The figure does not belong to Appendix A

Thanks for the comment. However, the numbering of the images is ruled by the copernicus latex template and is assigned automatically, to my knowledge. The ordering of the images is independent from the ordering of the appendixes. We hope that the technical editor can help in this respect.

Figure 9 caption: interpretation "and made a hook rain structure ... wind mixing" should not go to caption

thank you for the comment, we moved the sentence in the main text and reformulated the sentence at line 350 as follows: "Figure 9 d) shows a hook rain structure visible, possibly caused by downdraft wind mixing. The vortex structure was not visible in the original data (Figure 9 c)) and emerged from the noise after applying the correction on the mean Doppler velocity field."

Figure 12: I think, images from both radars should have the identical height axis range and identical color bar range and color map. This makes comparisons between W- and K-band much easier, even though it is not the objective of the paper.

We thank the reviewer for this comment. The goal of this paper is not to compare between the W and K band radars, but instead to display the measurements collected and show their potential. The high resolution adopted with the Wband radar can be incredibly beneficial for process studies and model evaluations, therefore we opted for showing it visibly. More detailed studies on precipitation that are planned by the main author will exploit the diverse information on precipitation coming from the usage of the W and K band frequencies. There the approach suggested by the reviewer will be exploited for the future analysis.

Line 399: It might be worth to discuss shortly the observed differences between both radars and how they complement each other. Different attenuation due to different wavelengths, different sensitivity, ...

In line with the previous reply, we think that an extensive discussion on this point would perfectly fit in a scientific publication focusing on precipitation more than in a data paper whose goal is to present a dataset, that can be used in various different ways, not necessarily exploiting the multifrequency approach. We actually will include such discussion in the planned publication on precipitation.

Line 434: just a comment: some airborne systems (unfortunately not HALO/HAMP) have an IRS/IMU as close as possible to the radar antenna
interesting thank you :)

Line 507: ... by alpha clockwise from North
corrected thank you

Line 507: for non-meteorologists you could add "(the direction where the wind is coming from)" this makes it easier to understand the minus signs in Eq. B1

The sentence has been modified as follows: " In the Earth reference system, the horizontal wind vector in absolute coordinates is given with the zonal component towards East, and the meridional component towards North and it represents the direction where the wind is coming from."

Line 514: If "yaw" psi is indeed ...
added, thanks

Line 523: heave is not discussed here

We removed the information on heave collected as last, because as suggested, is not relevant here.

Line 531 till end of page: check order of description of r_{rot} and v_{rot} , looks like repeating of definitions

We thank the reviewer for this comment, we rearranged the paragraph in a more linear way, we hope. Thank you for noticing.

Line 544, Eq. D1: should be $e_{p0} = \dots$ (?)
we added the definition of E_{po}

Line 547, Eq. D2: why not t_{final} for $\theta_{tbl,S}$

Thanks for the comment. The distinction between t_{final} and t_0 , the time when the table got stuck, follows from the fact that the time t_0 is measured by the stable table, and not by the ship time. The t_{final} time stamp is the closest time to at which the ship sensor collected observations of roll, pitch, yaw. There might be a small difference between these two times because they are measured by two different sensors. This is why we maintain the separation.

Acquistapace et al. describe in this paper the deployment, operation and data processing of two radar systems (W-band cloud radar and micro rain radar) on the research vessel Maria S. Merian during the EUREC4A campaign in early 2020. They describe the setup of the radars on a stabilization platform and the correction of measured Doppler velocities, both for times when the stabilization platform was operational and when it was stuck in an arbitrary position.

The manuscript is well written and clearly structured. The data set is easily accessible. I have a some comments and would recommend publication after addressing those.

We thank you the reviewer for the nice description of the paper.

General comments regarding the data:

It would be nice, if the data for ship motion was published along with the latest version of the radar data. Now, users have to access different data sets. And this also adds the danger of possibly using outdated radar data that are published along with the ship motion data (<https://doi.org/10.25326/156>) and could confuse some users.

Is there a way to access ship location information to use together with the hourly data?

What would users need to do if they want to know where the Maria S. Merian was located for a specific hourly data file?

The data for ship motion that have been included in the old dataset version contain the terms that we calculated for deriving the correction to the mean Doppler velocity, namely for each radar bin, the E_p vector, the time delay, the rotational velocity, the translational velocity, the course velocity and the wind velocity in the ship reference system. We also stored the correction term obtained from those and the denominator in the correction formula (see Formula 5). We did not include them in the latest version of the dataset because such data are not supposed to be used, and they could have created more confusion. They do not include the ship position, which is published on the AERIS data portal and publicly available at 1s resolution at this link https://observations.ipsl.fr/aeris/eurec4a-data/SHIPS/RV-MARIASMERIAN/dship/msm_089_1.tsg

To facilitate the data usage, we included the lat/lon information on the position of the ship in the daily dataset files (https://observations.ipsl.fr/aeris/eurec4a-data/SHIPS/RV-MARIASMERIAN/wband_radar/final_dataset/daily_intake/), where the lat/lon have been interpolated on the radar time resolution (3 s). The same was done also for the MRR data (<https://observations.ipsl.fr/aeris/eurec4a-data/SHIPS/RV-MARIASMERIAN/mrr-pro/>), but in this case the data were interpolated on 1s time resolution.

The dataset was created with the following concept: daily files (for both MRR and Wband) are the easiest to open, visualize and contain all the radar variables and the ship position that are of immediate interest for users. They are the main way to access the data and pick the case studies of interest. Once identified the exact hour of interest, radar interested users can open the specific hourly file if they are interested in deep advanced radar variables. In fact, all radar moments are stored in the daily file, and the hourly radar files contain in

addition only radar specific variables (full Doppler spectrum, sensitivity limit, mean noise level). For this reason, they are only for specific radar use. We hope to have clarified better the data structure.

Specific comments regarding the manuscript:

Figure 3: it is a bit unclear to me, what this figure should convey. The processing steps that are shown in the figure are not easily understandable by just looking at it. A lot of necessary information is given in the figure caption. One could think about adding these additional information from the caption also into the figure itself. The order in which the steps are mentioned in the caption does not match the order in the figure. I would suggest to either expand this figure a bit so that the processing steps are understandable by only looking at the figure or to remove the figure and expand the respective text section to thoroughly explain the processing steps. In the current state, the processing is a bit hard to follow between the figure, the caption and the text.

We thank the reviewer for the provided suggestion, which we took since we totally agree with the expressed opinion. We removed the figure and we expanded the text to describe the MRR data processing chain.

Line 157: "computer in a sealed container", what is the meaning behind this? What does the computer do? Is the information necessary? Also, does it have any impact that the container is sealed?

The computer is controlling the stable table behavior. It is positioned in a sealed container because, since it is standing outside, right under the stable table, it might be damaged by the atmospheric conditions. The information is necessary for future deployments, to properly install the equipment. The container does not impact the functioning of the computer.

Section 2.3: What are the limits of the stabilization platform compensation? I.e. maximum roll and pitch angles that can be compensated? Was this relevant during this campaign?

The report on the stabilization platform provided by Coulter et al, 2016 (<https://doi.org/10.2172/1253916>) describes the behavior of the table. In particular, the dimensions of this table allow for $\pm 30^\circ$ of pitch and $\pm 25^\circ$ roll, but as other tables, such extremes cannot be reached simultaneously (see Figure 2 in the report). The report also describes how the table responds to different sea conditions. Figure 4 shows that the observed conditions during our campaign were in the range of the conditions sampled in the testing phase, documented in the report. Therefore, we are confident that the table could work in a manageable regime of sea motions during EUREC4A.

Figure 5: this figure is hard to read in the current state. The ship's drawing in the background distracts from the coordinate axes plotted on top and is not necessary to understand the different rotation angles when the figure is first mentioned. I understand, that this figure is referenced later as well as an example on how the coordinate system is defined with respect to the ship. Could this figure be split into two figures for the different purposes?

We agree with the comment of the reviewer and we modified the figure

Line 193: "... time lag ΔT that varies with time between 1 and 4 s" is the variation

systematic (e.g. linear increase over the measurement duration)? Or are these random variations?

The variations we observed are quite random.

Line 214 and following: was the time correction done for each time step individually or was this applied to longer intervals?

The time correction was done for each time step individually. In particular, for each chirp time step. Within one time stamp of the radar, that takes 3 s, there are intermediate chirp times. The correction was applied to each chirp time stamp.

Line 373: "... cloud system identifiable as a flower type ..." It might be helpful for the reader to add a reference describing the different cloud organization names here.

Added, thanks for the comment.

Line 513: what is psi? If this is the yaw angle and the difference between psi and heading can be something other than zero, I don't understand why heading and yaw are used interchangeably in other parts of the manuscript (e.g. l167 (p9, second paragraph, third line), l523).

Psi is the yaw, and the difference between psi and heading is none. We have been erroneously using two terms because people use both. We will stick to yaw and remove the heading in the whole manuscript. Thanks for the comment.

Line 547, line 552: what is t_{fin} ? Should it be t_{final} ?

Yes, thank you, it is a typo and we corrected.

Figure A1: The vertical lines in A) and B) are only barely discernible or not at all. Maybe using another colormap (something like the ones used for the other figures in the manuscript) would help? The authors switch between lower case and upper case letters for the different figure parts between the figure itself and the figure caption and even within the figure caption.

Thank you for the comment, we updated the figure based on your suggestions.

Technical corrections

Line 8: hydrometeors -> hydrometeor

corrected

Line 33: time -> temporal

corrected

Line 35: setup -> setups

corrected

Line 127: add lat, lon as coordinates to the text

corrected

Line 188: I don't understand the use of the word "preliminary" here.

Removed, thanks for noticing

Line 475: "in agreement with what reported in" -> "in agreement with what was reported in"

corrected

Table 3: unit [deg C] not italic

corrected

The manuscript introduces the radar data sets collected during the EUREC4A campaign between trade wind region and tropical convergence zone on the research ship Maria S. Merian. The data set is unique and of high interest for the community. Necessary post-processing and some derived products published alongside the manuscript are presented. This manuscript deserves publication after correction of quite a number of small weaknesses and inaccuracies in the presentation. Questions to the editorial office rather than the authors arise from the use of webpage referencing and a reference to an unpublished manuscript.

We thank the reviewer for recognizing the importance of the dataset collected and we try of best to answer the comments and solve the inaccuracies and weaknesses found in the text.

General points:

The introduction and beginning of the section 2 left me confused about what to expect in this paper. Please be specific about what you will provide in this data set as early as possible. In the manuscript it only becomes clearer step by step. IWV is first mentioned in the beginning of section 2. LWP somewhat later, before IWV is detailed again. I would suggest to mention all these in the introduction and add a product table of all data set, their sampling rate, their expected accuracy, etc.

We included the derivation of the IWV estimations in the introduction. The modification can be found at line 31 in the new version of the manuscript: "The 89 GHz passive channel available in the W-band radar system allowed to characterize the columnar amounts of liquid water and integrated water vapor was retrieved only in clear sky conditions by means of a linear regression with co-located radiosoundings.". We refer to all the data products in section 2.1 and 2.2.

The authors should be clearer and more specific about the limitations of all their steps. Starting from active positioning, but also about the accuracy of all data sets published. ... Data without accuracy information is no data.

The accuracies of the roll, pitch and heave measurements from the stabilization platform are reported in section 2.4. Providing accuracies for radar data is actually a research topic itself due to the fact that such variables are non-linear functions of radar raw data. Acquistapace et al. 2017 (<https://doi.org/10.5194/amt-10-1783-2017>) investigated the sensitivity of the Doppler moments, with a particular focus on the skewness with respect to different spectral resolutions and integration times during identical time intervals to quantify the accuracy of Doppler higher moments. Recently a paper from Myagkov and Ori (<https://doi.org/10.5194/amt-2021-225>) investigated how to characterize random errors in dual-polarimetric spectral observations using error covariance methods. Radar moments like mean Doppler velocity, spectral width and skewness accuracies might be characterized similarly but as shown, this is a research paper itself and goes beyond the scope of this work.

Our data paper follows the path traced by similar older radar data papers like Neto et al. 2019 (<https://doi.org/10.5194/essd-11-845-2019>) where no discussion on accuracy or precision of radar reflectivity is mentioned. In our work, we aim at reporting the observations that were collected, discussing all their limitations and uncertainties throughout the text. We welcome the reviewer to suggest any possible approach that they have in mind to tackle the quantification of the accuracy for the derived radar variables.

In section 3.1 and 3.2 the nomenclature should be checked again. I have the impression that not all nomenclature is used correctly and some quantities are labelled in different ways. Please check, if all appendices are mentioned in the text. I only found references to App. A, C, D.

We checked through and we found some little discrepancies in the way the reference systems are called in the text and appendices, that have been fixed. We also noticed that appendices were not referred and we added that. We could not find any additional discrepancy. We thank you for the indication.

Minor and specifics:

Minor language editing will be needed as sentences are ill-constructed from time to time.

I.6: I would prefer not to use manufacturer product names in the abstract. The "PRO" in "MRR-PRO" is not needed and it's not introduced. Stay more general and leave out the "PRO" until you introduce the product in the "Experimental setup" section.

Thank you for the comment. We removed the PRO until the instrument was introduced and then we left the MRR-PRO.

I.20: "oceanic eddies". These show up uncommented and seem to be important. Can you add a sentence on what it is and why it is interesting?

We modified the sentence as follows: "The ship sampled some mesoscale oceanic eddies, that are circular fronts of sea surface temperature anomalies caused by oceanic turbulence, locally impacting near-surface wind, cloud properties and rainfall (Frenger et al., 2013).

L22: "OA". Please introduce.

We added the sentence: "Within EUREC4A, the Ocean-atmosphere component (EUREC4A-OA, <https://eurec4a.eu/overview/eurec4a-oa/>) was granted two research vessels (RVs) in the Atlantic sea south-east of Barbados to monitor the oceanic processes induced by large-scale oceanic eddies."

I.28: "MRR-PRO". As before.

Corrected

L33: "... spatial and time resolution of the entire precipitation life cycle." Of what? Daily, seasonal, global, local?

Here, we refer to the fact that both radars have high temporal (1-3s) and vertical (<10 m) resolution. Such high resolution allows to characterize and detect the processes occurring in small radar volumes, and therefore gives the ability to detect with a high sampling rate the precipitation cycle from the onset of rain until the moment in which that rain is reaching the sea surface or evaporating. The time scale of such process is hours, so it is not referred to any statistics, but more to the ability of detecting details of processes that were not discernible before.

I.42/43: "9 s". Where does this information come from? Measurement during the campaign? Does the "(Chris Fairall,...)" refer to them? Because the fact that a wavelength of 9 s needs measurements of at least 2 s to represent is mathematically obvious and would not need any support.

The 9s is precisely the information that Chris Fairall gave us from his experience in previous measurement campaigns. It refers to the longest integration time to be set in the radar for being able to correct for ship motions in the data. Although it might seem obvious, experimentally also other values like 2.5 s, or 3 s could seem acceptable. The threshold provided by Fairall was an important reference for setting up the measurement mode and define the chirp table. We reported in the publication because it might be helpful for future deployments as well.

I.47: "additional measurements onboard". Please add a "not presented/published here".
corrected

I.61-63: "Active remote ... satellite retrievals." This is a bit repetitive. Please remove.
Removed

I.74-77: "We calibrated ... factory calibration." This should be part of the instrument specific 2.1 and 2.2.
moved there, thanks.

I.81: "We launched ...". This reads as if you will also present these for a moment. Please be precise what to expect from this manuscript.

We used the verb "we launched" because the radiosondes operation were coordinated and organized on the RV by Acquistapace, i.e. the corresponding author of the paper. Moreover, the radiosonde data are used in the paper for retrieving the IWV as stated in the next sentence and are clearly referenced in the corresponding radiosonde paper, where Acquistapace is co-author. For all these reasons, we do think that the usage that is done in the publication of the radiosonde data is clearly stated and that it would sound weird to describe such data in a different way, given the above-mentioned conditions.

I.81: "descents". What is this?

As explained in Stephan et al, 2021, during EUREC4A not only the ascents of the radiosondes were used to collect observations of P, T, RH but also the descents. By means of a parachute located inside the balloon inflated from the ground, the sonde could fall gently after the breakup of the balloon at the highest point in the atmosphere, usually between 8 and 12 km. For each radiosonde thus, theoretically, we could obtain 2 profiles of the atmosphere.

I.83: More pieces pop up. You never said that you will provide an IWV data set, did you?

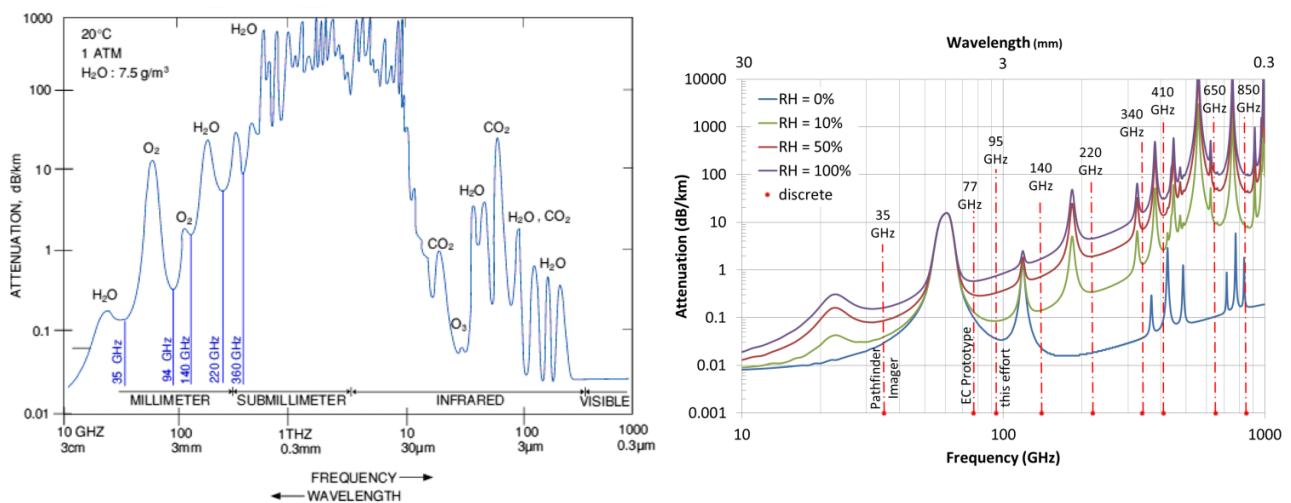
We corrected that and now it is written in the introduction, together with LWP.

I.107: The ANN retrieval of the manufacturer is not documented anywhere? No reference? The ANN retrieval is not yet published or documented by RPG.

I.114: Didn't you say that the atmosphere is relatively gas-transparent. How big are your errors? Usually other frequencies are used for IWV! Please comment. This probably only works, because of your dense and closely related radiosonde data? Which different radar "reflectivity values" are you talking about? Why plural?

The atmosphere is relatively transparent in the W-band (94 GHz), as shown in the figures below, but you can see that the response varies depending on the amount of humidity. This is why the passive channel at 89 GHz can somehow detect different IWV values in different conditions. However, much better retrievals can be obtained using a microwave radiometer and exploiting more channels between 22 and 32 and 51 to 58 GHz. Billault-Roux and Berne, 2021 (<https://doi.org/10.5194/amt-2020-311>) shows a similar approach using neural networks and also documents the lower accuracy of such approach based on a single frequency.

In our case, IWV is retrieved using a linear regression from IWV measurements from radiosoundings, collected during clear sky. To determine whether there are clouds or not, we use the Wband radar reflectivity, that is very sensitive to small cloud droplets. For a given time stamp to be considered clear-sky, all radar reflectivity observations collected in the vertical column of atmosphere should be < -50 dBZ. If such condition is met, then the time is classified as clear sky, and the radiosonde launched at that time is considered in the dataset for retrieving IWV.



sources for the figures: left : <https://bit.ly/3qQV6te> , right: <https://bit.ly/3kTfVQV>

I.132: I'm missing the products IWV and LWP.

LWP is mentioned among the integrated variables while the IWV is not stored in the output file because it has been derived just for the paper. The variable stored for future application is the brightness temperature at 89 GHz, as listed among the integrated variables.

I.142: Only this is where you should introduce the "PRO" part in MRR-PRO. "PRO" most likely is the "Professional" one. Only manufacturer terminology, but tell us.

As explained in the manufacturer page relative to the instrument, <https://metek.de/product/mrr-pro/> the PRO stands to indicate that the new version of the

MRR is the development of the old MRR with the technique of the MRR-2 that displayed higher performances and significantly improved parameter estimations. After introducing the PRO suffix, we prefer to keep it in the rest of the paper, to highlight that the instrument deployed belonged to the new generation of MRR instruments, with much higher capabilities.

I.146: This sentence seems awkward. Please re-phrase.

At line 146 we found this sentence: "Details on the ship motion correction algorithm and the interference filter are provided in section 3.2 and 3.4, respectively. The data are organized in daily files and the variables provided after the processing chain described in Figure 3 are reflectivity considering only liquid drops, equivalent reflectivity non-attenuated, equivalent reflectivity attenuated, hydrometeor fall speed, spectral width, skewness and kurtosis of the Doppler spectra, liquid water content, rainfall rate, rain drop size distribution, raindrop diameter weighted over mean mass, time, height, latitude and longitude.

We removed Figure 3 and explained the postprocessing more extensively in the text, followed by the list of variables.

Fig. 3: This is "method" not "experimental setup", isn't it? Wouldn't this better fit into 3.2 or 3.4?

We changed the title of the section to "experimental setup and data processing", thank you for your comment.

Tab.1: "spectral bins", "spectral resolution". This refers to the Doppler Fourier spectrum?

The number of spectral bins is the number of points in the fft transform to derive the Doppler spectrum. They correspond to the resolution of the xaxis along which the Doppler spectrum is displayed. The spectral resolution, in ms^{-1} , expresses what is the width in ms^{-1} of a single spectral bin. The ensemble of spectral bins composes the x axis along which the Doppler spectrum is displayed.

Please clarify.I.167: At the end of this section. What are the limitations of this positioning correction?

The limitations of the stabilization platform correction are stated in the sentence: "It must be noted that the stabilization platform can compensate for the rotation of the ship but it cannot compensate for the vertical movements along the vertical axis (heave, etc.) and the translations which occur because the ship rotates around its center of mass while the instruments are located elsewhere (see Section 3)"

In the rest of the paper, we discuss extensively the limitations of the table's ability to correct also for the rotation of the ship. The paper is almost entirely about that.

What is the frequency of correction steps? And how does this fit to expected and observed roll and pitch values and radar sampling? Where do the mentioned 35% come from? Please clarify.

Correction is applied to each chirp radar time stamp. This means that is it applied at a time resolution higher than the time resolution of the radar, that is 3s. Specifically, the chirp integration times are given in Table 3. Let's consider a given time stamp of the radar from T1 to T2. The corrections are applied:

- at $T_1+0.846$ for the chirp1 (radar range gates between 100 and 1233 m),
- at $T_1+0.846+0.786$ for the chirp 2 (radar range gates between 1233 and 3000 m)
- at $T_1+0.846+0.786+1.124$ for chirp 3 (radar range gates between 3000 and 10000m).

Note that the sum of the chirp integration times is 2.756 s, less than 3 s. The difference is an additional buffer time internal to the radar.

Roll and pitch values are provided with 1s resolution and the ones assigned for calculating the correction are the closest to the correction time stamp, as defined above, dependent on the chirp. It is clearly evident, thus, that using a higher resolution for the ship data (0.1 s instead of 1s) is crucial for improving the quality of the correction.

The 35% amount comes from the sensors of the table. Table measures roll and pitch as a function of time and whenever the table stops, no data are collected. By looking at the stable table time serie of data, one can easily calculate the amount of time the table stopped and the amount of time it was working.

Top paragraph on page 9 (line numbering mixed up): What is the frequency of MRU position measurements? You have not mentioned it anywhere.

It is 1s, it has been added. Thanks for the comment.

Page 9: There seems to be an 1,70 m offset between W-band and MRR. The image does not show this. Please comment.

Thanks for noticing the mistake. We assigned the same height to the two instruments, that is -17.40. The other measurement was taken when the stable table was off. The hydraulic pump that controls the table pistons, when turned on, pushes up the table and the instruments.

Fig 5: The combination of axes sketch and image in the back is confusing. First it looks as if you show a pitch angle. Then it takes some time to detect that you show an arbitrary combination of all three. Can you improve that? Maybe by changing the ship display and/or moving it away from the center of the figure? And where is the arrowhead of the y-axis?

Thank you for the comment. We tried in the new version of the manuscript to improve the figure. The arrowhead of the y axis, due to the 3d perspective, is not visible because it is in the dark circle. We modified the image.

I.200: "downdraft". The radar rather sees the downward motion of droplets and not the downdraft of the air. Please correct.

Cloud droplets have negligible fall velocities and therefore can be considered as air tracers. It cannot exist a downward motion of cloud droplets without a corresponding downward air flux. This is why generally we can talk about downdrafts also using radar observations. The measured fall speed is always a convolution of the air speed and the droplet fall speed. When drops have a non-negligible fall speed the radar measured velocity is a convolution of their fall speed and of the air velocity. Since rain while falling advects also air, there is also in this case a downdraft associated with the precipitation. This is why we talk of downdraft. We believe that this is the term that better represents the physical processes occurring in the situations observed in this paper.

L.215: Whole paragraph. Above you stated that you use a 20 min time window. Here you state that it is done for every radar chirp. Please explain at what frequency you derived the ΔT . And please, say a few words about likely reasons of the time offset. I can imagine that a time offset of several seconds between instruments develops over time. An erratic variation over the campaign is something I would not understand.

We thank the reviewer for the comment. The correction is applied to hourly files. For each hour, we estimate what is the time gap that every chirp has (chirp time stamps are clarified above). Such time gaps are different, and this is why we have to do it for each chirp. We estimate one ΔT for each chirp, so in total, 3 ΔT for every hour. To calculate a ΔT , we consider a 10 minutes (sorry for the mistake, not 20) time series of velocity measurements. The 10 minutes duration is necessary to guarantee enough data for the variance calculation, it corresponds to 200 time stamps (at 3 sec resolution). This choice is also due to the nature of these clouds, that often do not last more than 20 minutes in the observations. We average the time series over the chirp range gates, as described in the text, and calculate the variance. The ΔT minimizing the variance $\text{var}(\Delta V)$ is the delay for the chirp. The procedure is repeated for each chirp. Example time series are represented in Figure 6.

Regarding the reasons for the offset: We did all what was feasible to do on the ship to synchronize the instruments. The offset was observed and it is also visible in Figure 6 when comparing $\langle v_d \rangle$ and W_{signal} . We hypothesize that it might be due to the hardware connections and computer synchronization, but we cannot prove this. Also, as mentioned in the chirp time description, there is an additional 0.3 s time that is necessary for the radar to switch from one chirp to the other and to a new chirp cycle. Some variability can be due also to this internal radar processing time.

I.233/234: Didn't you just explain the same facts using the terms v_d and v_{hyd} in section 3.1? Please explain the difference once more, if needed. Otherwise please adjust nomenclature and remove repetitions.

We did not really understand to which facts the reviewer is referring to. In line 233-234 there is "The Doppler velocity measured by the radar is the projection of the particle's velocity vector on the radar line of sight. Therefore, the component of the velocity vector of the hydrometeors w_{signal} measured by the radar is positive when hydrometeors move upwards." We thought that it would have been good to state again this simple convention before entering in a long derivation of vectorial equations where the sign of the vertical axis is actually crucial. Is this the point the reviewer addresses and the sentence to remove?

The reason why the concept is repeated is the following. The complete vectorial equation for the velocity observed by the radar is equation 2. For calculating the time shift, the formula is simplified by neglecting all v_{radar} components other than v_{heave} . This approximation is valid since the other terms V_{course} and V_{rot} are much smaller than v_{heave} .

To clarify better this point, we added the following sentence in section 3.1 from line 200 in the new paper version :

"By comparing the heave rate (thin blue line) and $\langle V_d \rangle$ time series (thick red line in Figure 6) we can derive the time lag ΔT . Cloud droplets have a vertical speed of w_{hyd} . The ship

is moving vertically due to waves with w_{heave} . To a first approximation, we can neglect additional contributions to the vertical motion of the ship (for the full vectorial equation see treatment in section 3.2). The radar measures Doppler velocity v_d with respect to the instrument on the ship, hence $v_d = w_{\text{hyd}} + w_{\text{heave}}$.

We hope to have clarified the raised point. If not, we welcome suggestions from the reviewer.

I.259: Please comment on the need to label this data as "limited quality" here.

We thank the reviewer for the comment. In this part we just described the approach and we did not enter in the discussion of the quality of the correction. We just present how the correction is performed. Of course, such data have limited quality. However, this point is touched in the discussion on the plot of Figure 7, where the limitations of the approach when the table is not working are clearly displayed. This is why we did not opt for expanding on the data quality at line 259.

Page 13, bottom (line numbering broken again). "intensity" à "magnitude" of a vector?
We substituted intensity with magnitude.

L.268, eq 8: Reads like vectors are subtracted from a scalar?! It should be italic "v"s in the equation 8. On the other hand, it is not intuitive to label the z-component with another letter that "w"? Do you need another definition here? Please clarify and simplify nomenclature.

w is the z component. w_{signal} is coherently defined along z, while the other two terms are now in italics, representing the z components of the corresponding vectors. We believe the notation in this way is clear. We are sorry for the typo in the equation 8.

L.280: The first part of 3.3 reads slightly repetitive, apart from the horizontal wind influence. I think this part would better fit as last summarizing point in section 3.2.

I.284-292: This is why I'm still missing some information on accuracy of all these corrections in the different situations and some suggestions how to deal with them when using the data! Please add this information.

We decided to include the first part of 3.3 there as a sort of example application of the formulas derived in section 3.2. We believe it is better to separate the parts because section 3.2 is quite long already. We also think that it is important to discuss extensively the cases when the table is working and not working, supporting the discussion with Figure 7.

Regarding the accuracies: it would be fantastic to be able to provide an accuracy, because it would mean that we know the truth, regarding the corrections. Unfortunately, it is not so, and there is no reference to which we can compare to evaluate the correctness of the correction terms. We welcome any suggestion that can come from the reviewer on how to quantify the accuracy of the correction. From our side, we did our best to be rigorous and get the best data in the given conditions.

I.296: "Figure 7d)-h)." No d) and h) only show the platform status. e,f,g show the performance.

Now corrected to Figure 7 e)-g). We thank you for the comment.

I.302: "as described by looking at..." and Fig 8. I'm confused. I assume that this is a Fourier spectrum of the time series of vertical motion? Correct? In a certain cloudy range gate you can see the Doppler velocity fluctuation combined from particles' fall speed and ship motion w_{signal} . You cannot see the "vertical motion of the radar" v_{rad} which results from the ship motion, can you? Please mention equations 2, 7 and 8 and explain better. Fig. 8: I guess it should be frequency in "1/s" or better "Hz" on the x-axis? And the top label "periods" à "period".

The figure shows the fast Fourier transform of various quantities. In panel a) the black line is precisely the FFT of the nominator of the correction term in equation 6, i.e. $(V_{\text{wind}_s} - V_{\text{radar}}) * e_p$. Generally, V_{wind_s} has no vertical component (see appendix B), so the scalar product with E_p , when the table works, as it is the case for the figure 8, results in the z component of the vector v_{radar} , called v_{radar_z} . v_{radar_z} is the resulting velocity "felt" by the radar, and it is given by the composition of the various contributions along z of the terms given in equation 7, namely $V_{\text{trans}} = [0, 0, w_{\text{heave}}]$ and $V_{\text{rot}} = [v_{\text{rot}_x}, v_{\text{rot}_y}, v_{\text{rot}_z}]$. Such contributions are w_{heave} and v_{rot_z} .

We compare the FFT of the v_{radar_z} with the FFT of v_{rot_z} and w_{heave} , to demonstrate that the main contribution to the signal comes from w_{heave} . The FFT of the V_{radar_z} (black) is basically almost entirely overlapped to the one of the heave (translational velocity, purple line). It means that the heave rate is the main contribution to the vertical motion of the radar, that is on the ship.

In panel b) we compare the signal measured by the radar w_{signal} (black line here, while in panel a) it was represented by the yellow line) with the FFT of the velocity seen by the radar after applying the correction with the time shift v_{hydr} , while in panel c) it is the same thing but without the time shift correction. The comparison of panel b) and c) is presented to show the impact of the time shift correction. Basically, the frequencies due to the waves are not removed in panel c, while in panel b they are smoothed in the pink line.

We changed the labels in the figure according to the explanation above and we modified the caption in the new pdf version. We thank the reviewer for the comment that helped us to improve the description of the figure. We hope that now it can be easier to understand the showed results.

I.308: Is this the right range? 0.5 Hz is in the middle of your x axis!? See next point. 0.2 Hz lays on the right edge of the lower axis, in correspondence of 5 s period. The 0.5 Hz is not included in the range of displayed values.

I.310: This smooths the part between above 0.1 = 10 s period, correct? Above you state the range 0.1 to 0.5 Hz which would be period range 10 s - 16 s !?
I am not sure I am getting right the reviewer's comment here. The range 0.1 to 0.5 Hz corresponds to the range between 10s and 2s. We display the range between 10 and 5 s, which shows the mentioned increase of the spectra towards the Nyquist frequency.

I.311: Confusing sentence. And basically, nothing you need to put into an equation. Mean

speed multiplied with time is distance. Remove it.

We thank the reviewer for this comment. We tried our best to discuss the limitations of the presented approach and quantify them. The horizontal resolution for the radar is a distance, and therefore this is why it was expressed as a product of velocity times the integration time.

We reformulated removing the product and the sentence reads now as follows: "However, the 9 s smoothing degrades the average horizontal resolution of the Vhyd, mean by a factor of 9. For an average ship speed of 3 ms^{-1} , the resolution would change from 3 m to 27 m, resulting in a slightly higher resolution than the vertical 30 m one. However, daily maximum speeds for the ship can reach also 9 ms^{-1} , producing thus a coarser resolution."

I.333: "Prominence" is not a mathematical term. Please define.

Prominence is defined exactly after mentioning the word, as the peak's ability to stand out from the surrounding baseline of the signal. This is the most understandable definition, that is also referenced in the description of the python routines to calculate such quantity: https://docs.scipy.org/doc/scipy/reference/generated/scipy.signal.peak_prominences.html

L339: "lowest 600 m". Please give the reason why this assumption/ condition is justified.

The reason for asking for continuity in the lowest 600 m for the mean Doppler velocity of the MRR is that this is approximately the height of the sub-cloud layer, where rain gets out of the cloud and reaches the ground/evaporates. MRR detects only rain, and had strong interference problems above such height. This is the range of heights where we are sure that the MRR can detect rain, so it is worth comparing in this region.

I.342: "abrupt"? Please explain a bit. What reason could there be to accept 2 or 3? The same is true for point 3 in I.343. At least explain why, if they are all found empirically.

All these conditions are posed empirically to remove the signatures due to interference. The way in which the interference pattern affects the mean Doppler velocity of the MRR is displayed in figure figure A1). In figure A1a) the mean Doppler velocity field is continuous where there is signal, and is it a sequence of very high and low values where there is noise. If one calculates the difference of consecutive values along the profile, it is clear that peaks appear whenever nearby values change from extremely high to low or viceversa. When there are just a few peaks (3, or 4) , it might still be the case that there is a real signal in the column. However, when there are more than 8, we experimentally found that those columns correspond to interference (like in Figure A1a) at 1:50.

I.373: I wonder if "flower" has made it to general technical language already. Please explain EUREC4A slang.

We added a peer-reviewed paper published where the flower type of cloud is introduced.

L378: "difficult to quantify". Uuh. Isn't this what a data publication should provide? Best estimates of accuracy of the published data? If you cannot provide any accuracy you should not publish it at all? Please think about a way to provide some estimate on this.

We already answered this comment at the very beginning, stating that providing an accuracy to radar moments is itself a research topic out of the goal of this publication. We also provide information on the correction and its limitation, for what is feasibly possible, as describe in the comments above.

I.385: "Fig 12 b) displays clear areas". I'm confused. I don't see clear areas in b), I see them in a)? In addition, some explanation would be nice. Why is it clear in a) when I see large negative values in b)?

Thank you for the comment. We realized of an error in the plotting. We added and commented a new figure.

I.399: Please explain. LWP includes the rain. How does it contaminate the measurement?

Rain can make the radome of the 89 GHz channel wet, degrading the signal. Normally values above 1000 gm⁻² are flagged as rain.

EUREC⁴A's Maria S. Merian ship-based cloud and micro rain radar observations of clouds and precipitation.

Claudia Acquistapace¹, Richard Coulter², Susanne Crewell¹, Albert Garcia-Benadi^{3,4}, Rosa Gierens¹, Giacomo Labbri⁶, Alexander Myagkov⁵, Nils Risse¹, and Jan H. Schween¹

¹Institute for Geophysics and Meteorology, University of Cologne, Pohligstrasse 3, 50969, Koeln, Germany (DE)

²Argonne National Laboratory, 9700 S Cass Ave, Lemont, IL 60439, United States (US)

³Department Applied Physics—Meteorology, Universitat de Barcelona, Barcelona, 08028 (ES)

⁴Universitat Politècnica de Catalunya, Vilanova i la Geltrú, 08800, Spain

⁵RPG Radiometer Physics GmbH, Werner-von-Siemens-Straße 4, 53340 Meckenheim, Germany (DE)

⁶Universita' di Bologna, Via Zamboni 33, 40126 Bologna, Italy (IT)

Correspondence: Claudia Acquistapace (cacquist@meteo.uni-koeln.de)

Abstract. As part of the EUREC⁴A field campaign, the research vessel Maria S. Merian probed an oceanic region between 6° N and 13.8° N and 51° W to 60° W for approximately 32 days. Trade wind cumulus clouds were sampled in the trade-wind alley region east of Barbados as well as in the transition region between the trades and the intertropical convergence zone, where the ship crossed some mesoscale oceanic eddies. We collected continuous observations of cloud and precipitation profiles at unprecedented vertical resolution (7-10 m in the first 3000 m) and high temporal resolution (1-3 s) using a W-band radar and micro-rain radar (~~MRR-PRO~~MRR), installed on an active stabilization platform to reduce the impact of ship motions on the observations. The paper describes the ship motion correction algorithm applied to the Doppler observations to extract corrected ~~hydrometeors~~hydrometeor vertical velocities and the algorithm created to filter interference patterns in the ~~MRR-PRO~~MRR observations. Radar reflectivity, mean Doppler velocity, spectral width and skewness for W-band and ~~attenuated~~-reflectivity, mean Doppler velocity and rain rate for ~~MRR-PRO~~MRR are shown for a case study to demonstrate the potential of the high resolution adopted. As non-standard analysis, we also retrieved and provided liquid water path (LWP) from the 89 GHz passive channel available on the W-band radar system. All datasets and hourly and daily quicklooks are publically available. Data can be accessed and basic variables can be plotted online via the intake catalog of the online book "How to EUREC⁴A".

1 Introduction

Clouds and precipitation in the tropics are crucial for radiative budget and are responsible for climate prediction uncertainties (Bony and Dufresne, 2005). From 19 January 2020 to 19 February 2020, the "EUREC⁴A: A Field Campaign to Elucidate the Couplings Between Clouds, Convection and Circulation" campaign (Bony et al., 2017) took place in the Atlantic waters south-east of Barbados to test hypotheses on trade wind cumuli cloud feedbacks. Stevens et al. (2021) describe how the campaign's initial scope greatly expanded towards additional research questions, extending the campaign area and the number of scientific platforms involved. To understand the factors influencing rain formation, study the evolution of mesoscale oceanic eddies and their impact on air-sea interactions, and produce a dataset that can stand as a benchmark for future model evaluations and satel-

lite retrievals became complementary goals of the enlarged campaign. ~~The project~~ Within EUREC⁴A, the Ocean-Atmosphere component (EUREC⁴A-OA, <https://eurec4a.eu/overview/eurec4a-oa/>) was granted two research vessels (RVs) in the Atlantic sea south-east of Barbados to monitor the oceanic processes induced by large-scale oceanic eddies.

25 The RV Maria Sybilla Merian (MS Merian) was deployed in the southern part of the EUREC⁴A domain to investigate how mesoscale oceanic eddies impact oceanic circulation and their role in cloud and precipitation formation. The collaboration with the ARM Mobile Facility 2 (<https://www.arm.gov/capabilities/observatories/amf>) equipped the RV with a comprehensive suite of remote sensing instrumentation that could track each stage of the precipitation life cycle. A micro rain radar (~~MRR-PRO~~ MRR) and a cloud radar (W-band) were installed on a stabilization platform: while the W-band radar is sensitive
30 to a wide range of atmospheric scatterers from tiny cloud drops to raindrops, the ~~MRR-PRO~~ MRR can adequately describe the sub-cloud layer's rain evolution. The 89 GHz passive channel available in the W-band radar system allowed to characterize the columnar ~~amounts~~ amount of liquid water ~~-and integrated water vapor was retrieved only in clear sky conditions by means of a linear regression with co-located radiosoundings.~~ All W-band and MRR radar variables are listed in section 2.1 and 2.2.

The collaboration with ARM and the use of their stabilization unit allowed the compensation for ship motion and for the
35 first time, made possible to obtain essential Doppler observations at unprecedented spatial and ~~time~~ temporal resolution of the entire precipitation life cycle.

This radar suite represents one of the most advanced remote-sensing ~~setup~~ setups for measuring trade wind precipitation in and below the cloud. Ground-based cloud radar remote sensing has been used for long time to monitor the vertical structure of clouds and precipitation (Bretherton et al. (2010), Lamer et al. (2015), Leon et al. (2008), Kollias et al. (2007),), as well
40 as on ships (Zhou et al., 2015). In recent years, the potential of new observables like the Doppler spectra's skewness to detect precipitation forming in the cloud (Kollias et al. (2011b), Kollias et al. (2011a), Luke and Kollias (2013), Acquistapace (2017)) was demonstrated for fixed ground-based sites. However, ship-borne cloud radar Doppler measurements have not been exploited yet. A first analysis of the unique dataset of trade wind cumulus clouds and precipitation collected with the ~~MRR-PRO~~ MRR and the W-band radar on MS Merian is presented. Considering typical sea wave periods of 9 s, to obtain
45 Doppler observations at sea, integration times have to be chosen shorter than 1 s (Chris Fairall, personal communication). In the paper, we document how specific choices on the integration times of the instruments were taken, describing the measurement sampling strategy regarding spatial and temporal resolution.

The synergistic usage of the dataset collected on the RV will be crucial for tackling precipitation life cycle detection using a multiscale approach based on the additional measurements onboard not presented here: a water vapor Raman lidar and a wind
50 lidar from the University of Hohenheim, a cloud kite from the Max Planck Institute for Dynamics and Self-Organization of Göttingen (<http://www.lfpm.ds.mpg.de/MCO/ck.html>), that is a 250 m³ balloon able to fly up to 2500 m for in-situ observations of cloud and raindrop size distributions, 3d wind profiles, and eddy dissipation rates. When combining the W-band radar and the co-located in situ observations from the cloud kite, detailed description of the precipitation process and unique reference data for high resolutions model runs become available. The high vertical (7-10 m) and temporal (1-3 s) resolution adopted by all
55 the active remote sensing instrumentation below 2500 m will constitute an essential benchmark for future satellite missions like EarthCare (Illingworth et al., 2015), providing a detailed description of the atmospheric layer closer to the surface that is and

will be the most critical region to detect from satellite (Lamer et al., 2020). The 1-month precipitation data collected during the campaign also represents a vital evaluation dataset for Global Precipitation Measurement mission (GPM) performance at sea in the subtropics for shallow convection precipitation (Hou et al., 2014). The stabilization platform worked for approximately 60 65% of the time, while for 35% of the time it did not and we considered ship motion corrections for both situations. [Similar methods have been derived for airplane based measurements with Doppler measurements see e.g. \(Bange et al., 2013\).](#) The track followed by the RV MS Merian allows to characterize the latitudinal dependency on the cloud fields when moving from the subtropics towards the inter-tropical convergence zone and understand the impact of the sea surface temperature heterogeneities on the boundary layer (Laxenaire et al., 2018). ~~Active remote sensing instruments on a stabilization platform were installed on the RV MS Merian for the first time. The obtained dataset can be a reference dataset for further analysis like process studies, model evaluations and comparison of satellite retrievals.~~ We collected some lessons learned during the EUREC⁴A campaign with the hope of encouraging and facilitating future deployments of active remote sensing instruments on ships, given the strategic importance that such data might have.

The paper is organized as follows. Section 2 describes the experimental setup and the instrument characteristics. [Section 3](#) provides details on the data processing and on the removal of the interference pattern from the data, assessing the impact of the ship motion correction algorithm. Section 4 describes a case study of trade wind cumulus clouds and precipitation. We describe how to access data and processing scripts in section 5, while [Session-section 6](#) briefly collects the lessons learned and [section 7](#) summarizes the work.

2 Experimental setup [and data processing](#)

75 We positioned the radar equipment on the RV's top deck at around 20 m above sea level, as far as possible from the influence of sea spray (Figure 1). The W-band radar and the ~~MRR-PRO~~ [MRR](#) were mounted on the stabilization platform using two metal bars. To limit vibrations, we installed rigid support between the ~~MRR-PRO~~[MRR](#)'s pole and the W-band radar. ~~We calibrated the receiver of the W-band radar after installing it in the position shown in Figure 1. The receiver calibration is done using two calibration targets with two distinct brightness temperatures as described in Kuehler et al. (2017). The MRR-PRO comes with a factory calibration.~~ At installation, we synchronized the internal clocks of the computers controlling the radar equipment with the ship navigation system clock. Despite this effort, the time stamp synchronization suffered from a drift of the clocks with respect to the Global Positioning System (GPS) time of the ships inertial system [variable between 1 and 4 s](#) that we had to consider in the correction of the data for ship motions. From 19 January 2020 to 19 February 2020, the RV MS Merian sailed over a vast oceanic region spanning from 6°N to 13.8°N and from 51°W to 60°W (see Figure 2). We 80 launched 118 radiosondes and collected 38 descents to provide temperature (T), pressure (P) and humidity (q) profiles during the whole campaign (Stephan et al., 2021). This database was used to build a retrieval for integrated water vapor from the single passive 89 GHz channel available on the W-band radar. In the following, we will first describe the two radars followed by the stabilization platform and we will describe the Motion reference unit (MRU) and the ship reference system.

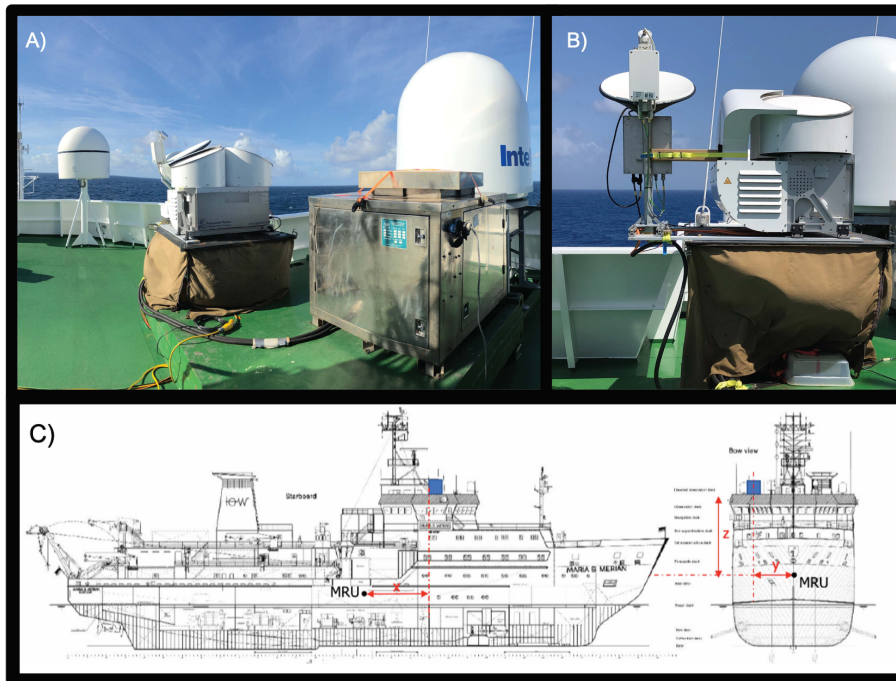


Figure 1. Instrument deployment on the RV MS Merian. A) View of the top deck (so called peil-deck): the hydraulic unit is visible on the right in the metal box, connected via multiple cables to the stabilization platform. B) The MRR-PRO MRR (left) and the W-band radar (right) fixed using two metal bars on the stabilization platform. C) Position of the instrument deployment with respect to the Motion Reference Unit (MRU) on the MS Merian: side view (left) and front view (right).

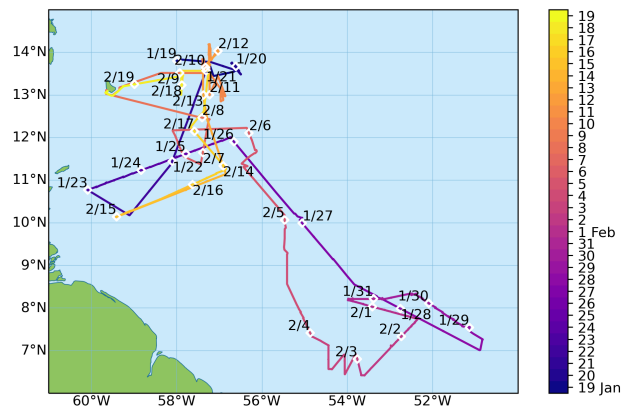


Figure 2. Ship track of the RV MS Merian during the EUREC⁴A campaign, from 19 January to 19 February February 2020.

2.1 W-band radar

90 The W-band radar is a frequency modulated continuous-wave (FMCW) 94 GHz dual polarization radar equipped with a radiometric channel at 89 GHz and is manufactured by Radiometer Physics GmbH (RPG), Germany. The small diameter of its antennas (0.5 m), one to transmit and one to receive, and its compactness (Table 1) make it a well suited instrument to be deployed in complex environments. K uchler et al. (2017) provided an extended description of the radar performance, hardware, calibration and signal processing procedures. [We calibrated the receiver of the W-band radar after installing it in the position](#)
95 [shown in Figure 1.](#) To protect the hydrophobic radome from hydrometeors, the radar is equipped with a blower for both antennas. The blower is able to produce a thin airflow with up to 20 ms^{-1} over the antenna radomes (K uchler et al., 2017). Users can set different range resolutions at different altitudes by providing the necessary parameters to the so called "chirp table", i.e. a table storing all the frequency modulation settings. Table 2 shows the chirp table definition adopted for this measurement campaign. We defined the chirp table to have a high vertical resolution below the inversion layer to focus on shallow cumulus
100 clouds (Table 2). This choice resulted in reaching a maximum detectable range of 10000 m to focus on high vertical resolution of the boundary layer clouds and the inability to measure high cirrus clouds. The range resolution from the sea-level to 1233 m was 7.5 m, while it was 9.2 m between 1233 m and 3000 m. Between 3000 m and 10000 m the range resolution was 34.1 m. We chose integration times of 0.846 s for heights smaller than 1233 m, 0.786 s between 1233 and 3000 m, and 1.124 s between 3000 m and 10000 m to make the ship motion correction effective. The total sampling time required to measure a full profile
105 resulted in around 3 s.

The embedded passive channel operates at 89 GHz with a bandwidth of 2 GHz and measures the calibrated brightness temperature (TB). In the W-band, atmospheric gases are relatively transparent. The absorption coefficient of atmospheric gases in the lower troposphere is of the order of 1 dB/km (Ulaby et al., 1981). In contrast, cloud liquid water produces a strong attenuation ($\approx 1 \text{ dB km}^{-1} \text{ g}^{-1} \text{ m}^3$, (Ulaby et al., 1981)) in this frequency band. Since the passive measurements are sensitive to
110 the presence of liquid water, the TB measured at 89 GHz can be used in a retrieval of liquid water path (LWP) (K uchler et al., 2017). The cloud radar continuously runs a statistical retrieval developed by the radar manufacturer. The retrieval is based on an artificial neural network (ANN), which approximates values of LWP for a given set of the observed TBs, surface temperature, relative humidity, pressure, and day of the year. For the ANN training, a dataset of atmospheric profiles was used. Since the ship was moving around Barbados during the campaign, data from several surrounding stations were combined in the dataset.
115 The dataset consisted of 3 radiosonde stations and one ERA-Interim reanalysis column (Dee et al., 2011). For more details in the ANN and the dataset used for it, please refer to the Appendix A and Table A1.

We obtained integrated water vapor (IWV) estimates by applying a single-channel retrieval in clear sky cases, defined as profiles where all W-band radar reflectivity values are smaller than -50 dBz. The retrieval is based on the quadratic regression between the 89 GHz brightness temperatures and the IWV estimated with the radiosoundings. We selected all radiosoundings
120 with relative humidity smaller than 97% in the entire profile launched when no cloud base was detected by the wind lidar on-board MS Merian. The IWV results from integrating the profile of specific humidity over height, and is associated with the mean 89 GHz brightness temperature calculated over 1 minute after the radiosonde launch.

The W-band radar data collected during the EUREC⁴A campaign have been post-processed using a software package, that includes processing and de-aliasing of compressed and polarized spectra. The code is an update and a subsequent restructuring of the first program version provided by Kuchler et al. (2017) and it is available at https://github.com/igmk/w-radar/tree/new_output_structure. No [liquid](#) attenuation correction has been applied to the data yet. The post-processing routine produces as output a technical data file including all radar specific variables, and a physical data file, available in two versions. One version (compact), [structured as daily files](#), includes:

- radar moments (equivalent reflectivity factor [\(from now on called reflectivity\)](#), mean Doppler velocity negative towards the ground, Doppler spectral width, Doppler spectrum skewness, Doppler spectrum kurtosis)
- coordinates (time, height, [latitude, longitude](#))
- integrated variables (liquid water path, brightness temperature at 89 GHz)
- surface variables collected by the meteo station attached to the radar (wind speed and direction, pressure, temperature, rainfall rate and humidity),
- general parameters (filecode/version number, compression flag)

The other version (complete radar data), [organized in hourly files](#), includes all the previous variables plus additional radar variables like the Doppler spectrum, the bin mean noise power and the sensitivity limit. In addition to the standard processing, we derived and added the mean Doppler velocity field corrected for ship motions to the variables listed above in both versions of the files. The compact version has been enhanced with Climate and Forecast (CF) conventions (<https://cfconventions.org/>) to allow online plotting using the EUREC⁴A book (<https://howto.eurec4a.eu/intro.html>). Section 3.1 and 3.2 describe the post-processing applied to the data and section 5 explains the available data products.

2.2 Micro rain radar

The Micro Rain Radar (~~MRR-PRO~~[MRR](#)) deployed on the RV MS Merian is a vertically pointing frequency modulated continuous-wave (FMCW) Doppler radar operating at 24.23 GHz, produced by the Meteorologische Messtechnik GmbH (Metek) (Peters et al., 2002) and owned by University of Leipzig. The instrument deployed was the latest version of the MRR, the so-called MRR-PRO, with antenna diameter of 0.6 m (Figure 1) [and comes with a factory calibration](#). Table 1 contains the main technical characteristics of the MRR-PRO and the specific settings adopted during the campaign. During the course, we observed interference of the instrument with the stabilization platform device. For this reason, we postprocessed the data independently instead of relying on the postprocessing of the manufacturer. [Initially the pre-processing converts the Doppler velocity range and performs the de-aliasing. Then, the interference is filtered out. The next step is to calculate the correction for ship motions for each time stamp and shift the Doppler spectra of the correction amount.](#) Details on the ship motion correction algorithm and the interference filter are provided in section 3.2 and 3.4, respectively. ~~The data are organized in daily files and the variables provided after the processing chain described in Figure ??~~ [Finally, all variables are derived by](#)

Table 1. Instruments technical specifications.

Parameter name	MRR-PRO	W-band
Operating frequency (GHz)	24.23	94
Operating mode	FMCW	FMCW
Modulation (MHz)	0.5 – 15	up to 100
Transmit power (W)	0.05	1.5
Antenna diameter (m)	0.6	0.5
No. of range gates	128	550
Range resolution (m)	10	7.5, 9.2 and 34.1
Resulting measuring range (m)	0 – 1270	100 – 10000
Temporal resolution (s)	1 s (10 s on some days)	3 s
Beam width (2-way, 6 dB)	1.5°	0.48°
Nyquist velocity range (m s ⁻¹)	±6.0 (0 to 11.9)	10.8, 7.3 and 5.1
No. of spectral bins	64	1024, 256 and 256
Spectral resolution (m s ⁻¹)	0.1889	0.0415, 0.0569 and 0.0398
Power (W)	500	400 (Radar), 1000 W (Blower)

standard post-processing of the shifted spectra. The variables are reflectivity considering only liquid drops, equivalent reflectivity non-attenuated, equivalent reflectivity attenuated, hydrometeor fall speed, spectral width, skewness and kurtosis of the Doppler spectra, liquid water content, rainfall rate, rain drop size distribution, raindrop diameter weighted over mean mass, time, height, latitude and longitude. Attenuation due to precipitation has been taken into account. More details on the derivation of the MRR-PRO variables can be found in Garcia-Benadi et al. (2020). ~~Steps of the processing applied for MRR-PRO data for the 1 s resolution dataset: from the manufacturer data, the pre-processing does the conversion of the Doppler velocity range and the de-aliasing, then the interference is filtered. Afterwards we apply the ship motion correction and then we derive the MRR-PRO variables from the shifted spectra. Finally the hourly files are merged in a daily file and the CF conventions are applied. Files are then structured in daily files and CF conventions are applied to make file readability easier. For the rest of the paper we refer to equivalent reflectivity non attenuated as simply reflectivity.~~

2.3 ARM AMF-2 stabilization platform

The stabilization platform from the US-Atmospheric Radiation Measurement (ARM) program Mobile Facility 2 (AMF2) was deployed on the RV MS Merian to reduce the impact of ship motions on the Doppler zenith pointing observations (Coulter and Martin, 2016). The system, built by Sarnicola Systems, is an active stabilization system, i.e., it compensates the ship motions by adapting the position of the table surface correspondingly so that the radar stays in a zenith pointing position. It requires 120 V power and ethernet connection to a computer in a sealed container to be operational. A Hydraulic Power Unit (HPU)

Table 2. Chirp table definition for W-band radar.

Attributes	Chirp Sequence (CS)		
	CS 1	CS 2	CS 3
Integration time (s)	0.846	0.786	1.124
Range interval (m)	100 - 1233	1233 - 3000	3000 - 10000
Range vertical resolution (m)	7.5	9.2	34.1
Nyquist velocity (ms^{-1})	10.8	7.3	5.1
Doppler velocity bins	512	256	256
Doppler velocity resolution (m-sms^{-1})	0.0415	0.0569	0.0398

170 (the cubic metal box on the right in Figure 1 a)) must be within 600 cm of the table and weights approximately 182 kg. The HPU supplies hydraulic fluid to manipulate the length of three legs positioned below the table's surface such that the table can compensate for a large range of roll and pitch angles of the ship. More information on the stabilization platform can be obtained at <https://www.arm.gov/capabilities/instruments/s-table>. Ship and table motion are monitored by 2 roll/pitch sensors, one located on the ship deck and the other in the center of the table itself. A predictive computer routine uses these values to

175 maintain the table in a geopotential level orientation at a constant height above the ships surface. Thus the table compensates for the rotational motions around the long axis of the ship (roll) and the short axis of the ship (pitch). [The Stabilization platform data revealed that the](#) table did not work for approximately 35% of the time. [The longest interval in which the stabilization platform was not working occurred between 1 and 5 February, when a connection cable was badly damaged and had to be exchanged. Around 17 February, we finally fixed the stabilization platform, and in the last 2 days the stabilization platform](#)

180 [worked continuously. Overall, we encountered the roughest sea conditions at the beginning of the campaign, and we had relatively calm sea conditions afterwards \(Figure 3\).](#) It must be noted that the stabilization platform can compensate for the rotation of the ship but it can not compensate for the vertical movements along the vertical axis (heave, etc.) and the translations which occur because the ship rotates around its center of mass while the instruments are located elsewhere (see [Section section](#) 3).

185 2.4 Motion Reference Unit (MRU) and ship reference system

When deploying a radar on a ship, vertical velocity measurements have to be corrected for ship motions, i.e. roll, pitch, yaw and heave (Figure 3). Roll and pitch variations cause the radar beam to be off-zenith and vertical range to vary with time; heave variations in time cause a vertical velocity offset and the vertical range to vary with time; the ship drift in the horizontal plane described by surge and sway may also have components in the direction of the radar beam if the radar is looking in any

190 direction tilted from the vertical relative to ocean. In this work, we will not calculate the surge and sway motions because we assume them to be negligible compared to the other terms.

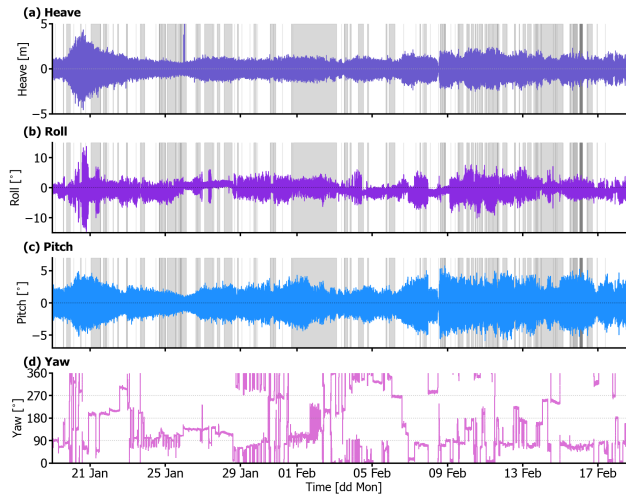


Figure 3. Time series of a) heave, b) roll, c) pitch and d) yaw of the RV MS Merian MRU unit during the EUREC⁴A campaign, from 19 January to 19 February 2020. Grey areas represent the periods of time in which the stabilization platform did not work.

All rotation angles are measured by the Motion Reference Unit (MRU) unit on the ship with a time resolution of 1 s. The MRU is a Kongsberg 'Seapath 320' system manufactured by Kongsberg SeaTex AS. The sensor uses 2 single frequency 12 channel GPS receivers for position and heading and provides roll, pitch, yaw(heading), and heave with an accuracy of 0.03°, 0.03°, 0.075° and 0.05 m, respectively (from <https://www.ldf.uni-hamburg.de/en/merian/technisches/dokumente-tech-merian/handbuch-merian-eng.pdf>). The MRU is mounted at the ships center of gravity to clearly separate between translatory and rotational movements of the ship. As the radars are not at the ships center of gravity, rotational movements of the ship lead to translation of the instruments. To calculate these movements it is necessary to know the position of the instruments with respect to the MRU. They were determined as vectors in the ships coordinate system as (Figure 4 and Figure 1 c)):

$$\mathbf{r}_{\text{W-band}} = [5.15\text{m}; 5.40\text{m}; \underline{-15.60-17.28\text{m}}]$$

$$\mathbf{r}_{\text{MRR-PRO}} = [7.18\text{m}; 4.92\text{m}; -17.28\text{m}]$$

In the MRU sensor's conventions, roll angle is positive when port goes up, pitch angle is positive when bow goes up, and yaw angle is positive clockwise from heading angle. The heading-yaw of the ship is given as the angle clockwise from north, and refers to the x-axis of the ship system. Finally, the coordinate for heave is negative for upward directions. The angle η is the angle between the initial position of the radar r (black vector in Figure 4) and its final position r' (blue vector) after a given motion due to the ship; η can be decomposed in terms of roll θ , pitch ϕ and yaw ψ (Figure 4). The stabilization platform worked for 65.35% of the measurement time and time in which the stabilization platform blocked itself in a random position for the remaining 35% of the time, are represented as grey areas in Figure 3. The longest interval in which the stabilization platform was not working occurred between 1 and 5 February, when a connection cable was badly damaged and had to be exchanged. Around 17 February, we finally fixed the stabilization platform, and in the last 2 days the stabilization platform

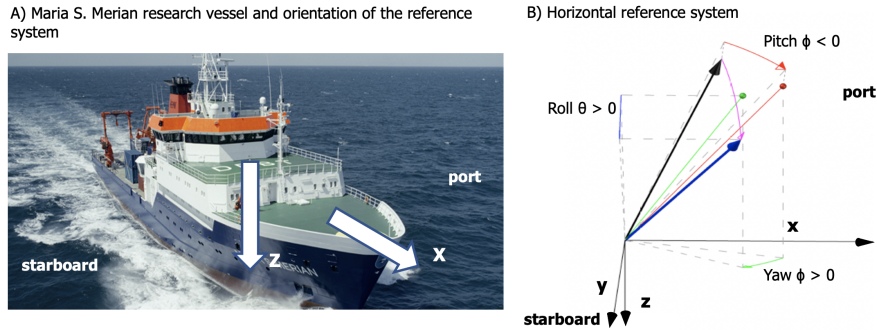


Figure 4. A) Port and starboard with respect to the RV MS Merian. B) Position of the radar and its tilting due to ship motions expressed in terms of roll, pitch and yaw of the ship. The original position is represented by a black vector (arrow), and the position after the movement is given by a blue arrow. The angle representing the rotation from the initial to the final position is η is the angle between the blue and the black arrow. The roll, pitch and yaw in which it can be decomposed are shown in blue, red and green, respectively. The solid red and green lines ending in filled circles of the same color represent the vector position after undergoing the rotations due first to pitch and then to yaw. The application of the rotation with respect to roll, would then bring the black array on the blue one. The sign with respect to the conventions indicated in the text is reported in the figure.

~~worked continuously. Overall, we encountered the roughest sea conditions at the beginning of the campaign, and we had relatively calm sea conditions afterwards (Figure 3).~~

3 Data Processing

This section describes the corrections applied to the data to obtain the final reference dataset. Subsection (3.1) describes the drift problem in time between the radar and the ship clock that both radar datasets undergo. Synchronization of the two is thus necessary ~~and preliminary~~ before applying any ship motion correction. Subsection (3.2) shows how to calculate the ship motion correction term for both radar datasets and subsection (3.3) assesses the correction algorithm. Finally, subsection (3.4) shows how to filter interference for MRR-PRO data.

3.1 Tackling time drift between ship and radar time stamps

At the beginning of the campaign, we synchronized the ship and radar clock. However, the ship and radar clock cumulated a time lag ΔT that varies with time between 1 and 4 s. To calculate the time-varying ΔT , we use the heave rate time series and the time series of the mean Doppler velocity averaged over the cloudy range gates $\langle V_d \rangle \langle v_d \rangle$ of each radar profile (see section 3.3 for more details on why using the heave rate time serie). For stationary radars, i.e. radars not moving in time, the mean Doppler velocity ($V_d v_d$) measures the mean velocity of the hydrometeors in the radar volume with respect to the radar that results as superposition of the air motion and the sedimentation speed of the drops. The average of $V_d v_d$ over the cloud geometrical thickness $\langle V_d \rangle \langle v_d \rangle$ fluctuates around zero in non-precipitating regions, because the sedimentation speed

of cloud droplets is negligible and updrafts and downdrafts present in the cloudy column are averaged out. In precipitation regions instead (for example in Figure 5 after 6:17:07), it becomes more and more negative, because of a larger and persistent downdraft. When the radar is moving (like on the ship), $\langle V_d \rangle \langle v_d \rangle$ additionally tracks the radar motion (Figure 5)).

220 By comparing the heave rate (~~thin-dashed~~ blue line) and $\langle V_d \rangle \langle v_d \rangle$ time series (~~thick-solid~~ red line in Figure 5) we can derive the time lag ΔT . Cloud droplets have a vertical speed of w_{hyd} . The ship is moving vertically due to waves with ~~w_{heave}^*~~ w_{heave} . To a first approximation, we can neglect additional contributions from the rotational movements of the ship (for the full vectorial equation see treatment in section 3.2). The radar measures Doppler velocity v_d with respect to the instrument on the ship, hence $v_d = w_{\text{hyd}} + w_{\text{heave}}$. Whereas w_{hyd} may vary with height due to up and downdrafts in the cloud, w_{heave} 225 is within one time step the same for all range gates. We average over all cloudy range gates within one time step to get $\langle V_d \rangle \langle v_d \rangle$. By doing so we partly remove the turbulent variation of w_{hyd} whereas w_{heave} remains unaffected ~~as it is the same for all range gates~~. From the ships MRU we have a time series w_{heave}^* , whose time stamp might be shifted against the radar time series. We calculate the variance ~~$\text{var}(\Delta v)$~~ $\text{var}(\Delta v_d)$ of the difference ~~Δv between $\langle V_d \rangle$ and $w_{\text{heave}}^*(t-Dt)$~~ Δv_d ~~between $\langle v_d \rangle$ and $w_{\text{heave}}^*(dt)$~~ over a time span of ~~20-10~~ minutes for different time shifts ~~Dt~~ dt . By doing so we get

230
$$\text{var}(\Delta v) = \text{var}(\langle V_d \rangle - w_{\text{heave}}^* \cdot (Dt)) = \text{var}(\langle V_d \rangle) + \text{cov}(w_{\text{hyd}}, dw_{\text{heave}}(Dt)) + \text{var}(dw_{\text{heave}}(Dt))$$

$$\text{var}(\Delta v_d) = \text{var}(\langle v_d \rangle - w_{\text{heave}}^* \cdot (dt)) = \text{var}(\langle w_{\text{hyd}} \rangle) + 2 * \text{cov}(w_{\text{hyd}}, dw_{\text{heave}}(dt)) + \text{var}(dw_{\text{heave}}(dt))$$

where ~~$dw_{\text{heave}}(Dt) = w_{\text{heave}}(t) - w_{\text{heave}}^*(t+Dt)$~~ $dw_{\text{heave}}(dt) = w_{\text{heave}}(t) - w_{\text{heave}}^*(t+dt)$. Ship movement w_{heave} and w_{hyd} are not correlated, i.e. the covariance term should become zero. The equation results then in:

$$\text{var}(\Delta v_d) = \text{var}(\langle w_{\text{hyd}} \rangle) + \text{var}(dw_{\text{heave}}(dt)) \quad (1)$$

For an optimal timeshift ~~Dt , the dt , that we call ΔT , the variance of the~~ difference dw_{heave} ~~and its variance become zero. For~~ 235 ~~all other timeshifts $\text{var}(dw_{\text{heave}}(Dt))$ is positive and accordingly for the optimal timeshift should get minimal (close to zero) and accordingly $\text{var}(\Delta v_d)$ is minimal.~~

We then applied the resulting time lag ΔT to the ship data and interpolated this shifted series to the exact radar time, obtaining the best correction term for each time stamp. We iterated the procedure for every radar chirp sequence since they all have different time stamps. Only after matching the time series of data from the ship and data from the radar, we could apply 240 the ship motion correction.

3.2 Derivation of the ship motion's correction formula

In the following we will derive the equations to remove ship movements from the observed radar Doppler velocities with and without a working stabilization platform. The algorithm applies to both radars. The only difference is that while for the W-band radar the correction was applied to the mean Doppler velocity, for the MRR-PRO the whole Doppler spectra is shifted by the 245 correction. We will adopt bold notation for vectors i.e. $\mathbf{v} = (v_x, v_y, v_z)$ where v_i are the components of the vector \mathbf{v} along the various axes.

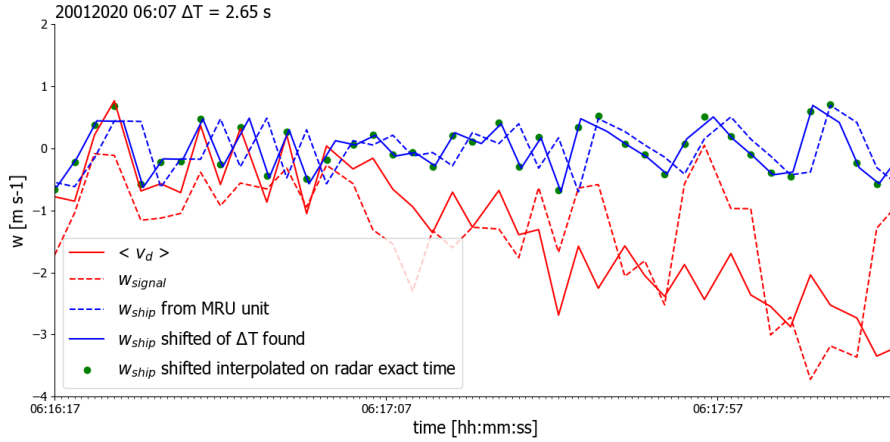


Figure 5. Example of time shift application calculated to obtain the best matched correction for ship motion from the 20 January 2020 over two minutes between 6:16:17 and 6:17:57 UTC. The **thin-dashed** blue line represents the vertical velocity measured by the ship w_{ship} . The **thin-dashed** red line is the mean Doppler velocity recorded by the radar at 1230 m, while the **thick-solid** red line represents $\langle V_d \rangle$, the mean Doppler velocity obtained by averaging together all cloudy pixels in each radar profile. The **thick-solid** blue line represents the ship velocity after applying the time shift of $\Delta T = 2.65s$, and the green dots represents the values of w_{ship} finally used for correcting for ship motion. They are obtained by cubic interpolation of the shifted ship velocity (**thick-solid** blue line) on the radar time stamps. In fact, they correspond to the values in the red lines, as expected after interpolation. In the first 7 seconds of the time series, a short train of 3 waves is clearly visible that matches the radar observed mean Doppler velocity values much better after the time shift.

The ship's coordinate system is defined by a right handed system with unit vectors \hat{e}_x , in direction of the bow, \hat{e}_y towards starboard and \hat{e}_z perpendicular to the decks downwards (Figure 4). With the ship moving in the waves this coordinate system is rotated by roll and pitch angles. This rotation is described by a rotational matrix \mathbf{R} (see [appendix C4 equation C4 in appendix C](#)). By applying the \mathbf{R} on unit vectors of the ship system we get a coordinate system with \hat{e}_z pointing vertically downward in the direction of earth gravitational acceleration g , and vectors \hat{e}_x and \hat{e}_y horizontally pointing in the direction of the ship's bow and starboard respectively. We call this system the horizontal coordinate system (Figure 4). $\hat{e}_z = [0, 0, 1]$ is the pointing direction of the \hat{z} axis of the horizontal coordinate system and points downward.

The radar observes Doppler velocities relative to its own movement along its radar beam and they are positive for movements away from the radar, i.e. upward for a vertical pointing instrument. The Doppler velocity measured by the radar is the projection of the particle's velocity vector on the radar line of sight. Therefore, the component of the velocity vector of the hydrometeors w_{signal} measured by the radar is positive when hydrometeors move upwards. The pointing direction of the radar in the horizontal system is denoted as \hat{e}_p . During times the stable table is working it is $\hat{e}_p = -\hat{e}_z$ (\hat{e}_p pointing upwards, \hat{e}_z pointing downwards). The velocity observed by the radar is the relative velocity between hydrometeors (\mathbf{v}_{hydr}) and the movement of the radar (\mathbf{v}_{radar}) projected onto the pointing direction of the radar (\hat{e}_p) that is:

$$w_{signal} = (\mathbf{v}_{hydr} - \mathbf{v}_{radar}) \cdot \hat{e}_p \quad (2)$$

where all vectors are given in the horizontal **ship**-coordinate system and the dot represents the scalar product. The movement of the hydrometeors can be decomposed in the horizontal system into a component along the vertical axis and one in the horizontal plane:

$$265 \quad \mathbf{v}_{hydr} = v_{hydr,s} \hat{\mathbf{e}}_z + \mathbf{v}_{wind,s} \quad (3)$$

where the term $v_{hydr,s}$ is the hydrometeor fall speed in the horizontal reference system (z component), and $\mathbf{v}_{wind,s}$ the horizontal wind vector in the horizontal reference system ([for the derivation, see appendix B](#)). Hence, we get:

$$w_{signal} = (v_{hydr,s} \hat{\mathbf{e}}_z + \mathbf{v}_{wind,s} - \mathbf{v}_{radar}) \cdot \hat{\mathbf{e}}_p \quad (4)$$

Now solving Eq. 4 for $v_{hydr,s}$ that is the hydrometeors fall speed in the horizontal reference system, we get:

$$270 \quad v_{hydr,s} = \frac{w_{signal}}{\hat{\mathbf{e}}_z \cdot \hat{\mathbf{e}}_p} - \frac{(\mathbf{v}_{wind,s} - \mathbf{v}_{radar}) \cdot \hat{\mathbf{e}}_p}{\hat{\mathbf{e}}_z \cdot \hat{\mathbf{e}}_p} \quad (5)$$

In the case of a working stabilization platform the radar pointing vector is exactly upwards and accordingly the scalar product $\hat{\mathbf{e}}_z \cdot \hat{\mathbf{e}}_p$ is equal to -1 as $\hat{\mathbf{e}}_z$ is pointing downwards. In the limit of a non moving ship we get

$$v_{hydr,s} = -w_{signal}$$

where the opposite sign is given by the fact that the ship reference system has an opposite z direction to the one in the radar convention. Finally in the common definition with falling hydrometeors having negative velocities we get:

$$v_{hydr} = -v_{hydr,s} = -\frac{w_{signal}}{\hat{\mathbf{e}}_z \cdot \hat{\mathbf{e}}_p} + \frac{(\mathbf{v}_{wind,s} - \mathbf{v}_{radar}) \cdot \hat{\mathbf{e}}_p}{\hat{\mathbf{e}}_z \cdot \hat{\mathbf{e}}_p} \quad (6)$$

The pointing direction of the radar $\hat{\mathbf{e}}_p$ in Eq. 5 changes depending on whether the stabilization platform is working or not:

- 275
- if the stabilization platform is working perfectly, we assume that $\hat{\mathbf{e}}_p = [0, 0, -1]$.
 - If the stabilization platform is not working the pointing vector of the radar is moving with the ship coordinates system. Accordingly $\hat{\mathbf{e}}_{p0}$ has to be rotated with the ships rotation matrix \mathbf{R} in the horizontal system and we get $\hat{\mathbf{e}}_p = \mathbf{R}^* \cdot \hat{\mathbf{e}}_{p0}^T$. The table typically got stuck at an arbitrary position and thus the radar is pointing in an arbitrary direction. We reconstruct this direction by taking roll and pitch at time t_0 just before the table got stuck and assuming that the radar was pointing at this moment vertically. Orientation of the radar in the ship system is thus $\hat{\mathbf{e}}_{p0} = \mathbf{R}^{-1}(t_0) * (-\hat{\mathbf{e}}_z)$ $\hat{\mathbf{e}}_{p0}^T = \mathbf{R}^{-1}(t_0) * (-\hat{\mathbf{e}}_z)$, which then translates to $\hat{\mathbf{e}}_p = [\hat{e}_{p0x}, \hat{e}_{p0y}, \hat{e}_{p0z}] = -\mathbf{R} * \mathbf{R}^{-1}(t_0) * \hat{\mathbf{e}}_z$ where \mathbf{R}^{-1} is the inverse matrix of \mathbf{R} (see Appendix C and D for more details).

The velocity vector \mathbf{v}_{radar} in Eq. 2 is composed of various contributions to the motion:

$$\mathbf{v}_{radar} = \mathbf{v}_{trans} + \mathbf{v}_{course} + \mathbf{v}_{rot} \quad (7)$$

285 where the velocities that add up to the radar movement are:

- **The translation velocity vector** $\mathbf{v}_{\text{trast}}\mathbf{v}_{\text{trans}}$ depends on the translation movements of the ship: heave, surge and sway (we neglect the surge and sway contribution), and it is given by

$$\mathbf{v}_{\text{trasttrans}} = [0, 0, w_{\text{heave}}].$$

(see appendix E for the derivation).

- **The course velocity vector** $\mathbf{v}_{\text{course}}$ is due to the travel of the ship along its course, and it is given by

$$\mathbf{v}_{\text{course}} = [v_s \sin \psi, v_s \cos \psi, 0],$$

where ψ is the yaw and v_s is the **intensity-magnitude** of the ship velocity vector (see appendix E for the derivation).

- **The rotation velocity vector** \mathbf{v}_{rot} describes the movement due to the rotation of the ship (roll, pitch, yaw) and the fact that the instruments are not deployed in the center of rotation but at distances $r_{\text{MRR-PRO}}$ and $r_{\text{W-band}}$ from it. Its expression is:

$$\mathbf{v}_{\text{rot}} = \frac{d\mathbf{R}}{dt} \cdot \mathbf{r}_{\text{MRR-PRO/W-band}}$$

(Appendix (C) for the derivation of the full expression).

3.3 Application of the correction and additional smoothing

290 When the table is working and the radar is pointing vertically all horizontal vector components vanish and the expression of the corrected hydrometeor velocity reduces to:

$$w = w_{\text{signal}} - \mathbf{v}_{\text{trast}}\mathbf{v}_{\text{trans}}_z - \mathbf{v}_{\text{rot}}_z \quad (8)$$

where $\mathbf{v}_{\text{trast}}\mathbf{v}_{\text{trans}}_z$ and $\mathbf{v}_{\text{rot}}_z$ are the z components of the vectors $\mathbf{v}_{\text{trast}}\mathbf{v}_{\text{trans}}$ and \mathbf{v}_{rot} . In this case, for calculating the velocity terms we need roll, pitch, heave rate. All these data are provided by the ship navigation system. Angles roll and pitch are necessary because the rotation of the ship moves the radar vertically. Course (**heading-yaw** and speed) are not necessary as the they are horizontal components not seen by the vertical looking radar.

When the table is not working, the pointing vector of the radar is most of the time not vertical and may have a horizontal component (scalar products of $\hat{\mathbf{e}}_p$ with horizontal vector components do not vanish). Accordingly course of the ship and horizontal wind may contribute to the signal. We therefore need additional parameters **heading-yaw** and speed of the ship and the horizontal wind above. The first two are provided by the ships navigation system. For the wind we used the output of dedicated ICON simulations run (Klocke, personal communication) over the EUREC⁴A domain to extract the horizontal wind profiles at the closest time and place of the ship, corresponding to the time when the table was not working. This type of correction affected 35% of the total measurement time. The low time resolution of the model output compared to the observations made this correction less accurate than the one applied for the 65% of the data in which the stabilization platform worked correctly.

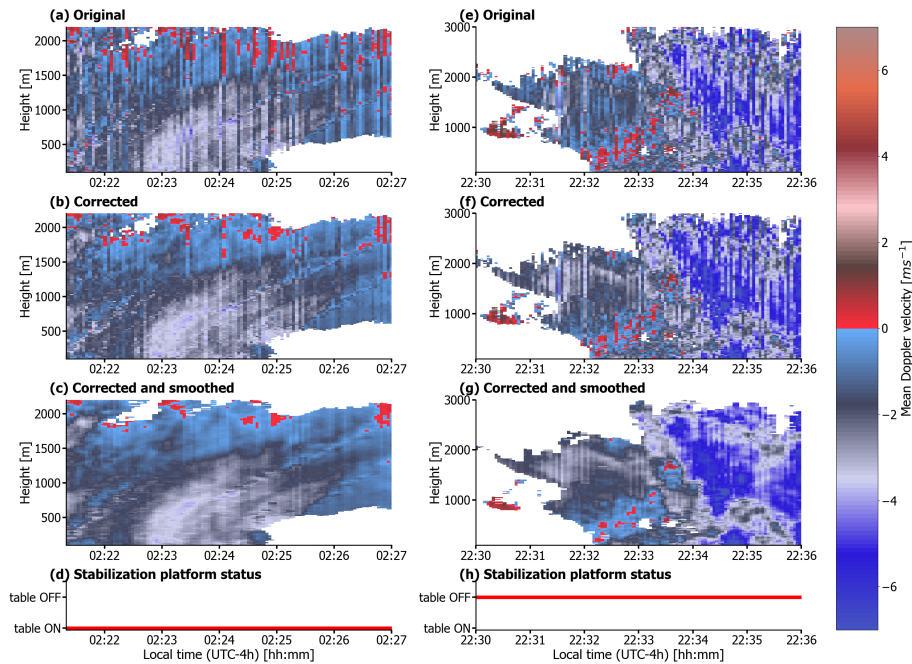


Figure 6. On the left, example of ship motion correction algorithm applied when the stabilization platform was working, on the 20 January 2020 from 2:21 to 2:27 LT (UTC-4h) for the W-band radar data with de-aliasing applied: a) Original mean Doppler velocity field without any correction algorithm applied, b) Mean Doppler velocity after application of the correction from ship motions, c) Mean Doppler velocity after application of correction from ship motions and smoothing (running mean over 9 s), and d) status of the stabilization platform. On the right, another example when the stabilization platform did not work, on the 12 February 2020 between 22:30 and 22:36 LT: e) Original mean Doppler velocity field without any correction algorithm applied, f) Mean Doppler velocity after application of the correction from ship motions, g) Mean Doppler velocity after application of correction from ship motions and smoothing (running mean over 9 s) and h) status of the stabilization platform.

An example of the application of the correction for ship motions when the stabilization platform is working is visible in Figure 6 a)-d), for the case of the 20 February 2020 between 2:22 and 2:27 Local Time (LT), with especially strong waves (compare with Figure 3). When comparing the original (Figure 6 a)) to the corrected mean Doppler velocity field (Figure 6 b)), one can quickly notice that many of the intense and frequent vertical bars disappear, providing a more homogeneous and continuous field. However, the correction cannot entirely remove the disturbances, as shown in Figure 6 b) by some visible vertical bars remaining despite the correction. Some possible reasons for the mismatch observed are the distance between the MRU sensor and the radar equipment, especially considering that we measured by hand the radar equipment's position. We are also assuming that the stabilization platform keeps the radar perfectly in zenith, but it is hard to quantify the accuracy of such hypothesis since a little error in the zenith alignment can produce disturbances. Moreover, the time lag quantification ΔT can be unprecise due to the reinitialization of the chirp generator of the W-band radar. Such time is random and adds an unknown uncertainty to the time stamps assigned to the measurements. Finally, the coarse temporal resolution of the MRU data makes an

interpolation to the radar data necessary. ~~Fig Figure~~ 5 nicely shows the rapidly changing w_{ship} which misses due to its coarse temporal resolution the real minima and maxima making an interpolation challenging. We applied a running mean over three time stamps (i.e., over a 9 s time interval) to account for these limitations (Figure 6 c)). The final signal obtained shows an almost continuous field in mean Doppler velocity.

Figure 6 ~~d)-he)-g)~~ show the correction performance when the table did not work, on the 12 February between 22:30 and 22:36 LT. Even if the final smoothing (Figure 6 g)) improves the v_d pattern compared to the field obtained when applying the correction algorithm only (Figure 6 f)), overall the performance is worse than in Figure 6 a)-c) and vertical stripes are markedly visible in all fields. We applied the time shift and the ship motion correction also to the MRR-PRO data obtaining similar results as will be shown in the section 3.4.

Figure 7 for one hour shows the impact of the time matching and of the correction applied to the signal in the frequency space. The heave rate is the main contributor to the vertical motion of the radar (Figure 7 a)), as described by looking at a cloudy range gate. The rotational components are approximately one order of magnitude smaller because the instruments are not too far from the center of mass of the ship, and the rotation of the ship moves the instrument not much along the vertical. For this reason, it represents the vertical velocity of the ship due to the waves, as previously stated. The frequencies of the waves at approximately 6 and 17 s (highlighted by the vertical dashed bars in Figure 7) are visibly removed in the FFT spectra of the corrected mean Doppler velocity only if the time shift is applied (compare Figure 7 b) and c)). Finally, the increase of the spectra towards the Nyquist frequency, between 0.1 and 0.5 Hz, indicates that there are higher frequencies above 0.5 Hz, folded back into this interval. Such frequencies do play a role that is not resolved by MRU nor by the radar itself. The final smoothing over the 9 s time window removes the high frequency components and it is thus crucial to obtain a better signal to noise ratio. However, the 9 s smoothing degrades the average horizontal resolution ~~:-given $V_{ship, mean}$ the mean ship speed, the degradation would change from $V_{ship, mean} * 1$ s to $V_{ship, mean} * 9$ s- of the $V_{hyd, mean}$ by a factor of 9.~~ For an average ship speed of 3 ms^{-1} , the resolution would change from 3 m to 27 m, resulting in a slightly higher resolution than the vertical 30 m one. However, daily maximum speeds for the ship can reach also 9 ms^{-1} , producing thus a coarser resolution.

3.4 Removal of Interference patterns and correction for ship motions for MRR-PRO dataset

The MRR-PRO electronics interfered with the ship instrumentation and with the stabilization platform electronics during the whole campaign. To be able to use the data collected, we removed the interference patterns using a noise removal mask. The interference draws periodical disturbances with peak intensity decreasing with height. Since the interference peaks are larger than the mean noise level calculated using the Hildebrand-Sekkon method by the manufacturer's processing (Hildebrand and Sekhon, 1974), multiple small peaks appear in the MRR-PRO spectra. The mean Doppler velocity and the spectral width of such noise spectra are random, depending on which noise peak is the highest (Figure A1).

The MRR-PRO dataset produced by the software of the manufacturer is initially processed with the MRR-PRO post-processing tool ~~developed by Albert Garcia-Benadi (publication in preparation) (Pre-processing and anti-aliasing steps in Figure 8)(Garcia-Benadi et al., 2021).~~ The algorithm allows to obtain de-aliased Doppler spectra over a physically realistic Doppler velocity range. For data with 5 or 10 s integration time, this tool is sufficient to remove the interference pattern. No

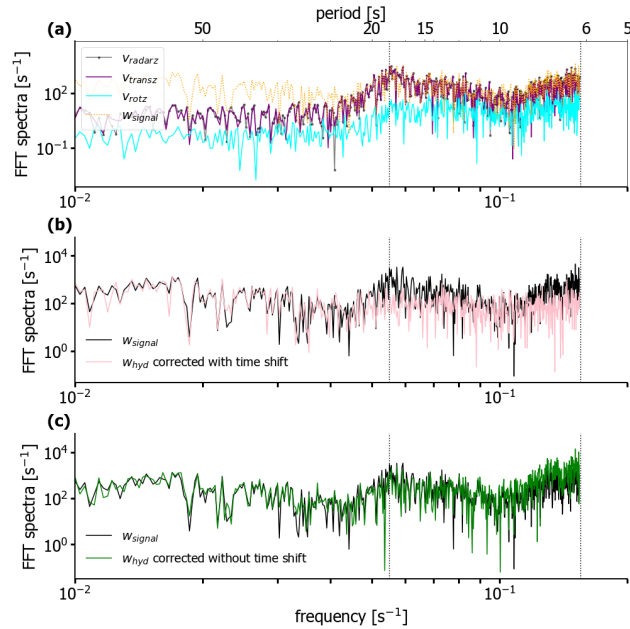


Figure 7. a) Fast-Fourier Transform (FFT) of the **ship-vertical velocity component of v_{radar}** and of its translational (purple) and rotational (cyan) components for one hour of data collected at a cloudy range gate located at 1605 m from the radar (**all terms along z in Eq. 7**). The **ship velocity v_{radar} FFT** highlights two main wave periods around 6 and 17 seconds, indicated by dashed vertical lines. In the total **ship-radar velocity along z** (black dotted line), the contribution of the rotational component is minor compared to the contribution of the translational component (heave). b) Comparison of the FFT of the **radar-uncorrected mean Doppler velocity** (black) **measured by the radar** and of the FFTs of the corrected mean Doppler velocity with time shift applied. The two main wave peaks disappeared in the corrected signal (pink line). c) Same as middle panel, but with the corrected mean Doppler velocity calculated without applying the time shift. In this case, the wave frequencies are not removed from the corrected signal (green line).

ship motion correction can be applied to those data because their integration time is larger or similar to the typical wave period (see Figure 7 a)) and Doppler variations due to heave motions are smoothed out. We resampled the data collected from the 19 to the 25 January 2020 with 5 s to a 10 s integration time, to reduce the impact of ship motions completely.

The post-processing of the data collected with 1 s integration time, i.e. from the 25 January to the 19 February 2020, is more complex (see Figure ??). For the 1 s resolution data, the tool from **Garcia-Benadi-Garcia-Benadi et al. (2021)** cannot remove the interference patterns as it did for the 10 s integration time dataset. Hence, to obtain Doppler spectra without interference we applied a noise removal mask (Interference filter in Figure 8) based on specific conditions:

1. We calculated for each spectrum the prominence of all its spectrum peaks, i.e. each peak's ability to stand out from the surrounding baseline of the signal. Then, we derived the difference between the maximum and minimum prominence and calculated their difference (ΔP). The difference is tiny for spectra containing only interference patterns and no signal from hydrometeors, while it is significantly larger for a Doppler spectrum detecting hydrometeor backscattering (see

for reference on Figure A1). Spectra affected by interference patterns were removed by selecting spectra with $\Delta P > 1 \text{ mm}^6 \text{ mm}^{-3}$, where the threshold value of one was determined empirically;

2. In addition, we posed a condition on the spatial continuity of mean Doppler velocity (mdv) in the lowest 600 m. The mdv obtained from spectra affected by interference shows very large random absolute values. Doppler spectra detecting hydrometeors produce continuous mdv field in space. We discarded all profiles where the difference of consecutive mdv values along the profile shows more than 8 abrupt peaks (threshold decided empirically).
3. We apply a spatial filtering to remove spurious noisy pixels: the filters excludes all pixels where $\Delta P > 1$ that have less than 3 adjacent neighbours fulfilling the same condition.

It is almost impossible to distinguish the signal due to hydrometeors from the one due to interference in the ~~attenuated reflectivity field Z_{ea}~~ reflectivity field Z_e of the original dataset. However, after applying the noise removal mask the hydrometeor signal becomes clearly visible (Figure 8 a) and b)). The time correction (see ~~Section~~ section 3.1) and post-processing tool from ~~Garcia-Benadi~~ Garcia-Benadi et al. (2021) were then applied to remove the time lag ΔT , de-alias and obtain a physically realistic Doppler velocity range for all Doppler spectra above the noise level (Anti-aliasing in Figure 8). Then, ship motion correction derived with the calculations presented in section 3.2 is applied and all the main MRR-PRO variables of interest are derived from the corrected Doppler spectra. Figure 8 ~~e) and d)~~ e) and d) show a ~~dynamic-vortex-structure~~ hook rain structure visible, possibly caused by downdraft wind mixing. The vortex structure was not visible in the original data ~~that~~ (Figure 8 c)) and emerged from the noise after applying the correction on the mean Doppler velocity field.

4 Characteristics of trade wind cumulus clouds and precipitation

To give an overview of the meteorological conditions encountered on each of the 32 days of campaign, Table 3 lists the daily mean atmospheric temperature (T2m), rain rate (RR), liquid water path (LWP), relative humidity (RH) and pressure (P) for each day of the campaign. They are collected at the radar base, which is approximately 20 m above sea level.

Figure 9 shows that the vast majority of the encountered liquid clouds have a LWP smaller than 100 gm^{-2} , with a median value of 11 gm^{-2} in agreement with Schnitt et al. (2017), who sampled the region between 10 and 20° N and -40 and -60° W in December 2013. Noise and gain drifts in the passive channel of the radar lead to positive LWP retrieved values even in clear sky conditions. These data have median and standard deviation of 1.2 and 5.4 gm^{-2} , respectively, which are within the retrieval uncertainty (about 30 gm^{-2}). The standard deviation of the clear sky distribution can be considered as a sort of uncertainty of the LWP values retrieved with the neural network algorithm, and can be used to correct the LWP values, as done in Jacob et al. (2019).

We compared the obtained IWV values with the IWV retrieved from GNSS by Bosser et al. (2021). The mean of the IWV retrieved from W-band radar single-channel retrieval is 31.7 kgm^{-2} , the median is 32.3 kgm^{-2} and the standard deviation of the distribution is 5.15 kgm^{-2} . The bias between the mean value of the IWV distribution from W-band and the IWV distribution from GNSS is 3.4 kgm^{-2} , which is consistent with the bias estimated with ground-based GNSS stations reported in Figure 9

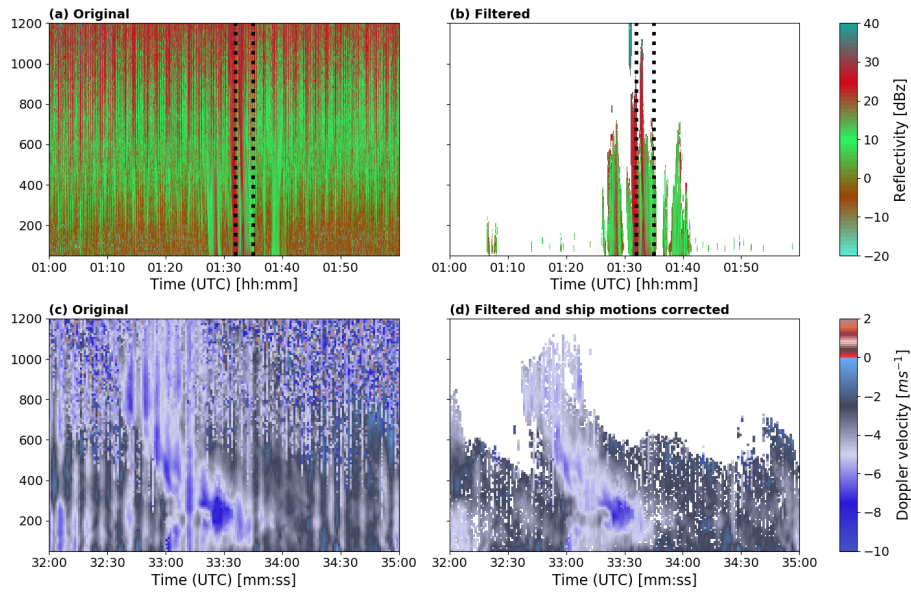


Figure 8. a) MRR-PRO attenuated reflectivity on the 13 February 2020 at 1:00 UTC after manufacturer processing, without any additional interference filtering or ship motion correction. b) Same as a), but with the noise removal mask applied. c) MRR-PRO mean Doppler velocity without any correction over a 2 min time interval selected from the time interval shown in a) between 1:32 and 1:35, and b) and highlighted with dashed black lines. Vertical stripes structures are visible due to ship motions. d) Same as c) but with interference removed and time shift and ship motion corrections applied to the data. The striped structure present in c) almost entirely disappeared **and made a hook rain structure visible, possibly caused by downdraft wind mixing.**

of Bosser et al. (2021). The spread between the GNSS and the radar derived values of IWV can be due to the strongly varying
 395 bias component that affects the GNSS IWV estimations from MS Merian (Bossler et al., 2021), as well as to limitations in the
 IWV single channel retrieval.

To show the full potential of the collected radar dataset, we display one case study of an extended precipitating cloud field
 occurring on 12 February 2020 from 15:30-00 to 17:00 UTC in the trade wind alley at about $^{\circ}13.5$ N and $^{\circ}57$ W. On that
 date, the ship encountered a cloud system identifiable as a flower type (Bony et al., 2020) using the corrected reflectances from
 400 Moderate Resolution Imaging Spectroradiometer (MODIS) TERRA (Platnick et al., 2003), with a diameter between 200 and
 250 km that generated precipitation during the afternoon (Figure 10 c)). When comparing the signals observed by the W-band
 radar (Figure 10 a)) and the MRR-PRO (Figure 10 b)), the different sensitivities of the two instruments become evident; while
 the W-band is capable of detecting cloud and precipitating hydrometeors, the MRR-PRO is sensitive to larger raindrops only.
 The interference patterns reduced the ability of the MRR-PRO to detect precipitation in a way that it is difficult to quantify.
 405 The W-band radar system collected echos in the first 2200 m showing the complex internal structure of the clouds. The cloud
 base detected from the W-band radar ranges between 750 and 1250 m, and does not exactly correspond with the LCL values

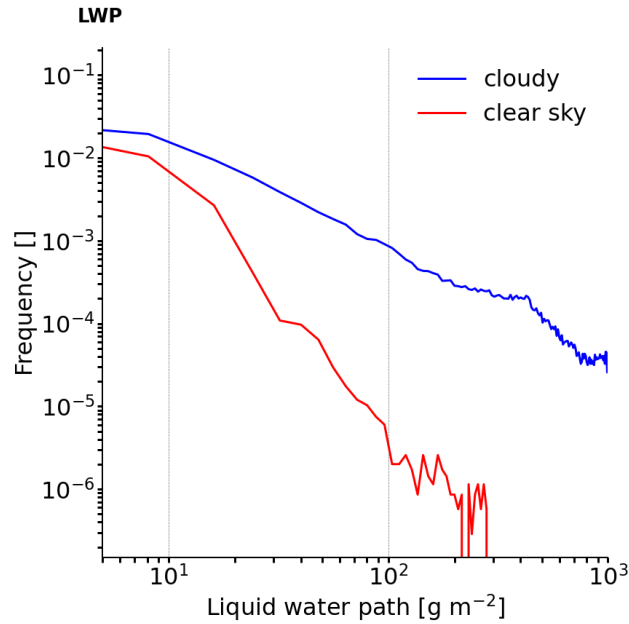


Figure 9. LWP distribution for cloudy (blue) and clear-sky (red) conditions, for the whole campaign.

(black solid line in Figure 10 a, b)) obtained for this case, while in non-precipitating conditions LCL is higher. Cloud top ranged between 1700 and 2100 m.

The high vertical resolution mode for the W-band radar (7 m up to 1230 and 9 m from 1230 m to 3000 m) detected distinctive features in the radar moments (Figure 11 a-d)). ~~Slanted filaments~~ Filaments of higher reflectivity between ~~16:25 and 16:30 at around 1000~~ 15:53 and 15:55 at around 800 m (Figure 11 a)) suggest a correlation of the size of the drops with air motions; Figure 11 b) displays clear areas in the cloud where larger mean Doppler velocities are associated with heavy rain. The spectral width field (Figure 11 c)) also benefits from the high temporal and spatial resolution. It shows patterns that suggest a correlation between large reflectivities and mean Doppler velocity values to large spectral width values. Finally, the skewness field shows patches of positive and negative skewness emerging from the noise. Further analysis of the Doppler spectra in precipitation is necessary to interpret these patches and exploit the skewness signatures (Acquistapace et al., 2019).

Also, for the MRR-PRO, the high vertical and time resolution allowed to reveal relevant structures in the lower precipitation field. Despite the small gaps caused by the filtering of the interference, the reflectivity (Figure 11 e)) shows a ~~general~~ decrease of the Ze values with decreasing altitude possibly due to evaporation and/or shear, ~~except for two moments, around 16:22 and 16:26 UTC, when the high observed Ze values correspond to high fall speeds of -4 ms^{-1} close to the surface~~ (Figure 11 f)). The case study highlights a large variability of fall speeds in the lowest 300 m, possibly connected with sub-cloud layer dynamics. The fall speed field can also trace such dynamics, as the vortex structure in Figure 8 d). ~~In contrast with the reflectivity and fall speed fields,~~ Also the rainfall rate ~~does not show a substantial variation~~ shows a substantial decrease as rain approaches the ground during the selected case study (Figure 11 g)). During the case study the stabilization platform worked continuously and

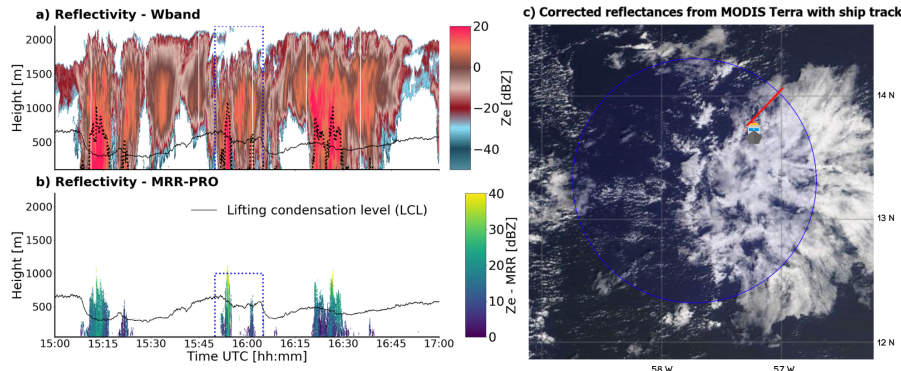


Figure 10. Overview of the selected case study of the 12 February 2020 between 15:00 and 17:00 UTC: a) Radar reflectivity from W-band radar. The black solid line represents the lifting condensation level calculated using the surface variables, while the black dotted line shows the highest detected signal from the MRR-PRO. The red dashed box represents the area shown in Figure 11. b) Attenuated reflectivity from MRR-PRO. c) Ship track on top of the corrected reflectance from MODIS Terra, displaying the flower cloud occurring in the area. The corrected reflectance from MODIS is a product that uses the bands 3 (479 nm, red), 6 (1652 nm, green), and 7 (2155 nm, blue) produced in near real-time (NRT) to provide natural looking images. The blue circle represents the orbit of the HALO aircraft. The image is taken at 16:03 UTC. Source: <https://observations.ipsl.fr/aeris/eurec4a/Leaflet/index.html>

425 the LWP registered ~~very high values~~ high values and saturated ($LWP > 1000 \text{ gm}^{-2}$) under rainy conditions. Note that values above 1000 gm^{-2} should not be considered as reliable because of contamination due to rain.

5 Data availability

The data presented in this paper can be accessed at AERIS repository and on the ARM database in NetCDF format, under (<https://doi.org/10.25326/235>) (Acquistapace et al., 2021c). This DOI was assigned to the new version of the dataset, produced
430 after fixing a bug in the standard post-processing script and correcting the LWP neural network dataset. In the dataset:

- technical radar variables were removed and stored in hourly technical files that can be accessed upon email request to the manuscript’s corresponding author.
- A Doppler velocity variable has been added to facilitate the usage of the Doppler spectrum variable.
- A compact data version suitable (including ~~only radar moments~~ radar moments and geolocation) for the EUREC⁴A intake
435 catalog has been produced following CF conventions. In the EUREC⁴A book now available at <https://howto.eurec4a.eu>, some example codes on how to read the data and plot basic quantities are available for users. More support will be added here in the future.

Auxiliary dataset used for correcting for ship motions can be found at <https://doi.org/10.25326/156> (Acquistapace et al., 2021b), together with the outdated version of the radar data.

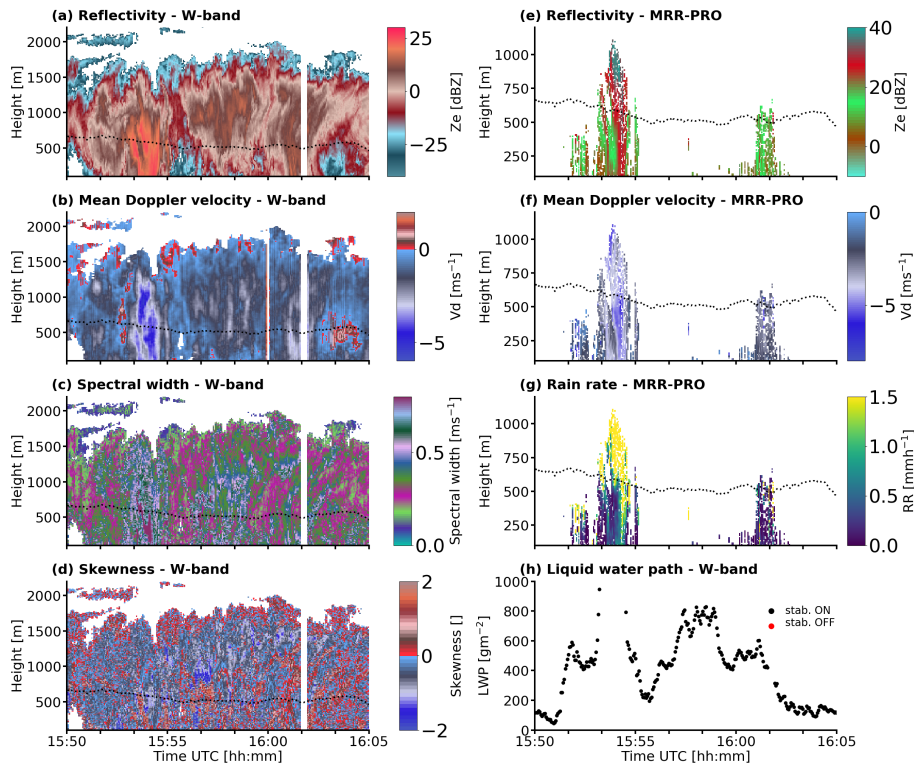


Figure 11. Detail of the case study shown in Figure 10 for W-band variables a) Reflectivity, b) Mean Doppler velocity, c) Spectral width, d) Skewness and for MRR-PRO variables e) Attenuated reflectivity, f) mean Doppler velocity, g) Spectral width. LWP and stabilization platform status are displayed in h).

440 The MRR-PRO data can be accessed at AERIS repository and on ARM databases (<https://doi.org/10.25326/233>) (Acquistapace et al., 2021a). Data are organized in daily NetCDF files. Also this dataset is following CF conventions and is included in the EUREC⁴A intake catalog with example codes for basic operations with the data.

445 Finally, the code used for post-processing the W-band radar data is published on github (<https://github.com/ClauClouds/w-radar>). The post-processing software for MRR-PRO data ~~will be published in a devoted publication (Garcia-Benadi, 2021, in preparation)~~ is published in [Garcia-Benadi et al. \(2021\)](#). The code for ship motion correction and interference filtering and for deriving the plots of the paper can be accessed at zenodo <https://doi.org/10.5281/zenodo.5014088>. All the data are visualized in hourly and daily plots on the quicklook browser <https://bit.ly/3xLkb9b>. For improving the data visualization (Zeller and Rogers, 2020), we created color palettes using the Colorgorical tool (Gramazio et al., 2017), and we used them for all plots of the quicklook browser as well as for many of the graphics of this publication.

450 6 Lessons learned

As underlined in the introduction, we experienced various challenges deploying active remote sensing instruments on the MS Merian research vessel. For encouraging and facilitating future deployments on ships, we collected some issues we encountered that future technological developments could solve.

The ship motion correction algorithm described here has also been tested on the radar data collected on the Meteor research vessel, where the ship navigation system data used 0.1 s (10 Hz) time resolution. We noticed that increasing the time resolution of the ship position data from 1 Hz to 10 Hz is beneficial for the ship motion correction. Spectral analysis of the data from MS Merian indicates that there are components of the ship movement at frequencies above 0.5 Hz which had to be filtered out by a simple gliding average smoothing operator. We therefore recommend using 10 Hz for future campaigns.

A significant limitation to the exactness of the correction came from the need to synchronize the radar clocks with the GPS time from the ship. This is necessary to assign the right correction to be used for the measurements. The synchronization problem is a well-known issue for aircraft measurements, and more research is needed to tackle this point. At least for ship purposes, a possible solution could come from including a high-resolution sensor in the radar that can tell the radar inclination and heave for each radar partial chirp sequence time stamp with high precision. Currently W-band radar position data (inclination, and elevation) are provided with the time resolution of the total sampling time, which is approximately 3 s and is too poor for an effective correction of ship motions.

Finally, we strongly recommend a preliminary test phase to the campaign, as we did in this work. The time spent before the campaign in testing the instruments allowed us to take care and solve small details that could have strongly affected the measurement quality, like the vibration of the pole or the best setup for the computer connections onboard the RV. We experienced interference problems on the ship. Interference is always hard to detect and to solve, but we recommend making some test measurements with all instruments and checking the raw data obtained. In our case, the MRR-PRO interference was not visible on the quicklooks of the control system, but it significantly impacted the observations. In a test phase, interference could be tackled and possibly solved.

7 Conclusions

This paper presents the W-band and MRR-PRO dataset collected on the MS Merian research vessel during the EUREC⁴A campaign between 19 January and 19 February 2020. We installed and operated two radars on the stabilization platform deployed on the ship with the collaboration of the ARM AMF2. The suite of instruments constituted an advanced setup for studying the precipitation life cycle in the tropical region and the first deployment of Doppler instrumentation on the RV MS Merian. The ship sampled a broad oceanic region between 6° N and 13.8° N and 60° W to 51° W. The data collected provide a precious characterization of the trade region and the transition from the trades to the intertropical convergence zone. The ship sampled some mesoscale oceanic eddies, ~~and the~~ that are circular fronts of sea surface temperature anomalies caused by oceanic turbulence, locally impacting near-surface wind, cloud properties and rainfall (Frenger et al., 2013). The collected

observations will provide vital information to understand the impact of sea surface heterogeneities on the marine boundary layer.

We developed an algorithm to correct the Doppler observations from ship motions and successfully applied it to the W-band dataset. The algorithm initially calculated the time shift between the radar time stamps and the ship navigation system time to identify the radar position with respect to the motion reference unit as best as possible. It then applies the correction term to the mean Doppler velocity. For the *MRR-PRO* data, in addition to the ship motion correction algorithm, we also developed advanced post-processing techniques to filter out interference problems between the *MRR-PRO* and the stabilization platform. We first removed the interference pattern, and we then applied the correction directly to the Doppler spectra. Then, we used the standard post-processing to derive the moments and the other rain-related variables from the corrected Doppler spectra.

The corrected fields remove most of the typical striped pattern due to heave motion in the mean Doppler velocity (W-band) and fall speed (*MRR-PRO*) that ship motions cause to Doppler measurements. The correction for ship motion was applied to the entire dataset. However, for 35% of the data, the stabilization platform did not work. We corrected this data subset using the horizontal wind profile extracted from NWP ICON-LEM model runs and horizontal ship velocity.

A unique feature of the dataset is the high temporal and vertical resolution; the time resolution is 3 s (W-band) and 1 s (*MRR-PRO*). Below 3000 m, i.e., where most of the cumulus liquid clouds develop, the range resolution of the W-band is 9 m or 7 m, while the one of the *MRR-PRO* is 10 m. The profiles of the W-band radar moments detected with unprecedented detail showed characteristics patterns that will be explored in future works, especially for what concerns the spectral width and skewness. *MRR-PRO* variables like the fall speed contain important detailed information on the dynamical evolution of the rain in the sub-cloud layer and its interaction with the dynamics. We exploited the passive 89 GHz channel available on the W-band radar to retrieve LWP in cloudy conditions and IWV in clear-sky situations. The LWP retrieval is a neural network retrieval provided by the radar manufacturer, while the IWV is derived from a single-channel quadratic regression between the 89 GHz brightness temperatures obtained in clear-sky and the IWV measured by the radiosoundings launched at the exact times. We assessed the IWV retrieval by comparing it to the IWV estimations obtained by GNSS (Bossler et al., 2021). We found a bias of 3.4 kgm^{-2} , in agreement with what [was](#) reported in Bossler et al. (2021).

The high resolution of the collected datasets and the possibility of synergies with the other instrumentation on board, i.e., Raman lidar, wind lidar, cloud kite, make the described observations a benchmark dataset for future analysis as model studies and evaluations, comparing satellite retrievals and process studies. We made the data public and accessible on the AERIS and the ARM database platforms to achieve these purposes. Moreover, we also made the data accessible online via the EUREC⁴A intake catalog, and hourly and daily quicklooks are available online for browsing into the data.

Future work will focus on improving the quality of the correction: when the wind lidar corrected dataset from MS Merian will be published, it will provide horizontal wind profiles for the entire campaign and thus allow to obtain a better correction for the 35% of the dataset collected when the stabilization platform did not work.

515 *Video supplement.* The corresponding author realized a short video from the campaign that was approved by the ship board and is available online at the following link: <https://www.youtube.com/watch?v=EdWNS77qMNA>

Appendix A: LWP retrieval using neural network

This appendix describes the neural network retrieval developed to retrieve LWP from the single passive channel at 89 GHz of the W-band radar, exploiting radiosoundings launched in the region of the campaign. The dataset consisted of the 3 radiosonde stations collocated in Grantley Adams International Airport (Barbados), International airport of "Le raizet" (Guadeloupe) and Piarco international Airport (Trinidad) and the one location from the ERA-Interim reanalysis (see Table A1). All available profiles from Jan 1994 to Dec 2016 were used. In total, there were 41588 profiles. We used 29111 (70%) randomly chosen profiles for the ANN training and 10% of the dataset for the validation. We used the remaining 20% for the retrieval evaluation (test dataset). For each profile, we calculated the LWP following Löhnert and Crewell (2003). A radiative transfer model was used to simulate TB values at 89 GHz. The absorption of oxygen and water vapor was calculated according to Rosenkranz (Rosenkranz, 1998, 1999). The absorption by liquid water was calculated using the Rayleigh scattering approximation and the model from Liebe et al. (1991) and Liebe et al. (1993).

We used as input variables for the ANN training the simulated brightness temperatures (TB), day of the year, near surface temperature, relative humidity, and pressure. The values of temperature, relative humidity, and pressure closest to the surface were taken from profiles. The calculated LWP was used as the target variable. The input and the target variables were normalized using the min-max function. The ANN consists of two layers: a hidden layer with 5 neurons and an output layer with one neuron. The hyperbolic tangent is used as an activation function for all neurons. The standard error backpropagation algorithm was used for the training. After the training, we evaluated the retrieval using the test dataset. The retrieval root mean square error (RMSE) is 33 gm^{-2} . During the radar operation, the ANN uses TBs measured by the passive channel and measurements of the surface temperature, relative humidity, and pressure from the weather station.

535 Appendix B: Calculation of the wind speed in the ship horizontal reference system $\mathbf{v}_{wind,s}$

In the Earth reference system, the horizontal wind vector in absolute coordinates is given with the zonal component towards East, and the meridional component towards North and it represents the direction where the wind is coming from. If it has a speed $v_{wind,E}$ and a direction indicated by α with respect to the clockwise from North, it can be written in Cartesian coordinates as:

$$540 \mathbf{v}_{wind,E} = [-v_{wind,E} \sin \alpha, -v_{wind,E} \cos \alpha, 0] \quad (\text{B1})$$

After applying the rotational matrix of ship motions, the ship horizontal coordinate system (see Fig. 4) has:

- x axis to the heading-yaw of ship, horizontal, perpendicular to the gravity acceleration g ,
- y axis to the starboard of ship, right side, horizontal, perpendicular to g ,

– z axis downward in direction of g

545 If yaw ψ is indeed given relative to heading, the equations describing the wind in the ship horizontal reference system are:

$$\begin{aligned}\mathbf{v}_{wind,s} &= [u_{ship}, v_{ship}, 0] \\ &= v_{wind,E}[-\sin(\alpha - \psi + 90), \cos(\alpha - \psi + 90), 0] \\ &= v_{wind,E}[-\cos(\alpha - \psi), \sin(\alpha - \psi), 0]\end{aligned}\tag{B2}$$

because the ship horizontal coordinate system is rotated clockwise by $\psi - 90$, and the y-axis of the ship has opposite direction with respect to the Earth reference system.

~~We can hence re-write Equation 6 as:-~~

550 $\mathbf{v}_{hydr} = [0, 0, w] + v_{wind,E}[-\cos(\alpha - \psi), \sin(\alpha - \psi), 0]$.

Appendix C: Calculation of the rotation vector \mathbf{v}_{rot}

Let's define η the rotation angle resulting from ship motions. The rotation matrix \mathbf{R}^* associated with a generic rotation η , is the product of the rotation matrices associated with the roll, pitch and yaw, in the way the angles provided by the MRU sensor on the ship are defined. The prescribed order for the MS Merian is roll (θ), pitch (ϕ), ~~heading (yaw)~~ yaw (ψ), ~~heave~~. The general expression for the rotation matrix is hence given by:

$$\mathbf{R}^* = \mathbf{CBA}$$

where \mathbf{A} is the rotation matrix for the roll, \mathbf{B} is the rotation matrix for the pitch, and \mathbf{C} is the rotation matrix for the yaw. The expressions for \mathbf{A} , \mathbf{B} , \mathbf{C} are:

$$\mathbf{A} = \begin{pmatrix} 1 & 0 & 0 \\ 0 & \cos\theta & -\sin\theta \\ 0 & \sin\theta & \cos\theta \end{pmatrix}\tag{C1}$$

555
$$\mathbf{B} = \begin{pmatrix} \cos\phi & 0 & \sin\phi \\ 0 & 1 & 0 \\ -\sin\phi & 0 & \cos\phi \end{pmatrix}\tag{C2}$$

$$\mathbf{C} = \begin{pmatrix} \cos\psi & -\sin\psi & 0 \\ \sin\psi & \cos\psi & 0 \\ 0 & 0 & 1 \end{pmatrix}\tag{C3}$$

The expression for \mathbf{R}^* is:

$$\mathbf{R}^* = \begin{pmatrix} \cos \psi \cos \phi & \sin \phi \sin \theta \cos \psi - \sin \psi \cos \theta & \sin \phi \cos \theta \cos \psi + \sin \psi \sin \theta \\ \sin \psi \cos \phi & \cos \psi \cos \theta + \sin \psi \sin \phi \sin \theta & -\sin \theta \cos \psi + \sin \psi \sin \phi \cos \theta \\ -\sin \theta & \cos \phi \sin \theta & \cos \phi \cos \theta \end{pmatrix} \quad (\text{C4})$$

560 The **heading** term ψ is necessary only when the stabilization platform gets stuck and we ignore it when stabilization platform works. We call \mathbf{R} the rotational matrix obtained when neglecting ψ , that applies for 65% of the data. Rotational movement of the ship leads to translational movement of the instrument because it is not located in the center of mass of the ship. The location of the radar with respect to the center of mass at any moment of the rotation is $\mathbf{r}_{rot} = \mathbf{R} * \mathbf{r}_{radar}$. ~~Its velocity is the derivative with respect to time : $\mathbf{v}_{rot} = d/dt(\mathbf{R} * \mathbf{r}_{radar}) = d\mathbf{R}/dt * \mathbf{r}_{radar}$, with x, y and z the coordinates of the radar location vector on the ship.~~

$$565 \mathbf{r}_{rot} = \begin{pmatrix} x \cos \phi + y \sin \phi \sin \theta + z \sin \phi \cos \theta \\ y \cos \theta - z \sin \theta \\ -x \sin \theta + y \cos \phi \sin \theta + z \cos \phi \cos \theta \end{pmatrix} \quad (\text{C5})$$

The vector \mathbf{r}_{rot} does not contain ψ because we ignore yaw when table is working. The velocity variations of the stabilizing system with respect to the MRU are described by the derivative with respect to time of the vector $\mathbf{r}_{rot} = \mathbf{R} \cdot \mathbf{r}_{radar}$:

$$\mathbf{r}_{rot} = \begin{pmatrix} x \cos \phi + y \sin \phi \sin \theta + z \sin \phi \cos \theta \\ y \cos \theta - z \sin \theta \\ -x \sin \theta + y \cos \phi \sin \theta + z \cos \phi \cos \theta \end{pmatrix}$$

570 ~~The vector \mathbf{r}_{rot} does not contain ψ because we ignore heading when table is working.~~ that is $\mathbf{v}_{rot} = d/dt(\mathbf{R} * \mathbf{r}_{radar}) = d\mathbf{R}/dt * \mathbf{r}_{radar}$, with x, y and z the coordinates of the radar location vector on the ship.

Adopting the point as a symbol for the temporal derivative, the rotational velocity results in:

$$\mathbf{v}_{rot} = \begin{pmatrix} -x\dot{\phi} \sin \phi + y(\dot{\phi} \cos \phi \sin \theta + \dot{\theta} \sin \phi \cos \theta) + z(\dot{\phi} \cos \phi \cos \theta - \dot{\theta} \sin \phi \sin \theta) \\ -y\dot{\theta} \sin \theta - z\dot{\theta} \cos \theta \\ -x\dot{\theta} \cos \theta + y(\dot{\theta} \cos \phi \cos \theta - \dot{\phi} \sin \phi \sin \theta) - z(\dot{\theta} \sin \theta \cos \phi + \dot{\phi} \sin \phi \cos \theta) \end{pmatrix} \quad (\text{C6})$$

Appendix D: Calculation of $\hat{\mathbf{e}}_{p0}$ and $\hat{\mathbf{e}}_p$

575 When the stable table stops working it leaves the table and thus the instrument in an arbitrary orientation denoted by a fix vector $\mathbf{e}_{p0} \cdot \mathbf{e}_{p0}$ in the (rolling and pitching) ship system. This vector can be transformed to the horizontal system by multiplication with rotation matrix \mathbf{R}^* (see Appendix C) as $\hat{\mathbf{e}}_{p(t)} = \mathbf{R}^* * \mathbf{e}_{p0} \cdot \hat{\mathbf{e}}_p(t) = \mathbf{R}^* * \mathbf{e}_{p0}$:

$$\hat{\mathbf{e}}_p \hat{\mathbf{e}}_p(t) = \mathbf{R}^* * [\hat{e}_{p0x}, \hat{e}_{p0y}, \hat{e}_{p0z}] \quad (\text{D1})$$

\mathbf{e}_{p0} where $\mathbf{e}_{p0} = [\hat{e}_{p0x}, \hat{e}_{p0y}, \hat{e}_{p0z}]$ can be calculated from the position in which the table was when it got stuck. The stabilization platform angles at the time t_0 when the table got stuck can be obtained as follows. For the roll

$$580 \quad \theta_{tbl,S}(t_0) = \theta_{ship}(t_{final}) - \theta_{tbl,S}(t_{final}), \quad (D2)$$

for the pitch

$$\phi_{tbl,S}(t_0) = \phi_{ship}(t_{final}) - \phi_{tbl,S}(t_{final}) \quad (D3)$$

and for the yaw:

$$\psi_{tbl,S}(t_0) = \psi_{ship}(t_{final}) \quad (D4)$$

585 where $\theta_{tbl,S}(t_{final})$, $\phi_{tbl,S}(t_{final})$ and $\psi_{tbl,S}(t_{final})$ are the last recorded positions of the stable table relative to the ships deck as recorded in the raw data files of the stabilization platform. t_{final} is the closest time of the ship time serie to the time t_0 when the table got stuck, in which there was a record of ship data. The point vector $\hat{\mathbf{e}}_{p0}$ can then be obtained as:

$$\mathbf{e}_{p0} = \mathbf{R}^{*-1}(t_0) * [0, 0, -1] \quad (D5)$$

where the inverse rotational matrix \mathbf{R}^{*-1} is calculated as:

$$\mathbf{R}^{*-1} = \mathbf{A}^{-1} \cdot \mathbf{B}^{-1} \cdot \mathbf{C}^{-1},$$

where \mathbf{A}^{-1} , \mathbf{B}^{-1} and \mathbf{C}^{-1} are the rotational matrices associated to the roll, pitch and yaw angles of the table at the time t_0 :

590 $\theta_{table_S|t_0}$, $\phi_{table_S|t_0}$ and $\psi_{table_S|t_0}$. The expressions of the matrices \mathbf{A}^{-1} , \mathbf{B}^{-1} and \mathbf{C}^{-1} can be obtained from the expressions of \mathbf{A} , \mathbf{B} , \mathbf{C} , by using negative angles.

The final expression for the pointing direction is:

$$\hat{\mathbf{e}}_p = \mathbf{R}^* \cdot \mathbf{e}_{p0} = \mathbf{R}^* \cdot \mathbf{R}^{*-1}(t_0) * [0, 0, -1] \quad (D6)$$

where \mathbf{R}^{*-1} is provided by the definitions above.

595 **Appendix E: Calculation of \mathbf{v}_{course} and $\mathbf{v}_{trast}\mathbf{v}_{trans}$.**

The course vector \mathbf{v}_{course} is determined by the ship velocity \mathbf{v}_s and its heading-yaw ψ . We decided to calculate the ship velocity by deriving the UTM coordinates given by the MRU-GPS system of the ship with respect to time. We hence get:

$$\mathbf{v}_{course} = [v_s \sin \psi, v_s \cos \psi, 0] \quad (E1)$$

The translation vector $\mathbf{v}_{trast}\mathbf{v}_{trans}$ that the ship undergoes has three components:

600 – heave: it is the variation of the z position due to the waves and it is provided by the MRU system. Its projection along the radial beam might be of the order of the hydrometeor fall speed.

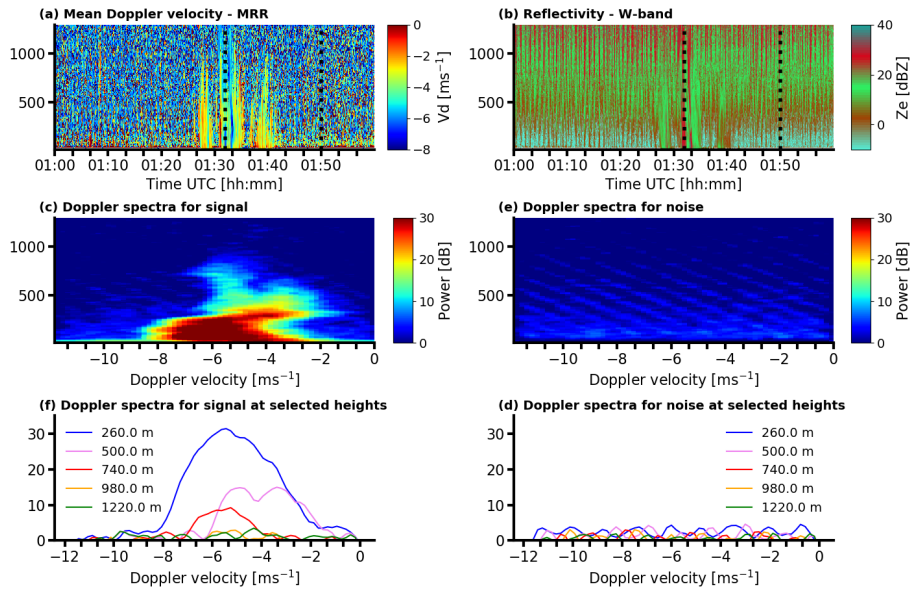


Figure A1. Interference in the MRR-PRO data: a) mean Doppler velocity for one selected hour. The black vertical lines correspond to the selected times for plotting the spectra shown in panels [\(c\)](#) to [\(f\)](#). b) Same, for reflectivity. c) Height spectrogram of MRR-PRO Doppler spectra collected at [81:2533:4000](#) UTC during rain, where the horizontal white dashed lines indicate the heights selected for plotting the spectra shown in [\(e\)](#) and [\(f\)](#). d) same for Doppler spectra collected at [81:3250:4000](#), in the noise. [\(e\)](#) Doppler spectra collected along the vertical selected profile for rain [at various heights](#). [\(f\)](#) Doppler spectra collected along the vertical selected profile for noise, [at various heights](#).

– surge and sway are the short term variations of the position in the x/y direction compared to the ship velocity slowly varying term. They are not provided by the MRU system but can be derived from the ship velocity data by applying a short time averaging. We will neglect their contribution, since it should be small as long as the point vector $\hat{\mathbf{e}}_{p0}$ does not deviate more than 10° from the vertical direction.

We can then write:

$$\mathbf{v}_{\text{trasltrans}} = w_{\text{heave}} \cdot \hat{\mathbf{e}}_{\mathbf{z}} = [0, 0, w_{\text{heave}}] \quad (\text{E2})$$

where $\hat{\mathbf{e}}_{\mathbf{z}}$ is the unit vector $\hat{\mathbf{e}}_{\mathbf{z}} = [0, 0, 1]$ and the heave velocity results in being positive downwards.

610 *Author contributions.* Claudia Acquistapace took care of the data curation, the funding acquisition and the project administration for the deployment of the instruments on the ship. She also developed the software used for the post-processing and prepared the manuscript original draft. Jan H. Schween was involved for methodology and conceptualization of the post-processing algorithms; Nils Risse and

Giacomo Labbri were involved in the data visualization. Alexander Myagkov helped to specify observational settings for the W-band radar, applied and described the LWP retrieval developed by RPG, and assisted in checking W-band radar data. Albert Garcia Benadí was involved in the programming and the execution of the MRR-PRO post-processing while Rosa Gierens took care of the programming and the execution of the standard W-band radar data processing. Susanne Crewell initiated the deployment of the instrumentation and provided constructive feedbacks on the manuscript structure and organization; Richard Coulter provided supporting algorithms to operate the stabilization platform and covered a supervision role in the execution of the mentioned codes. All co-authors reviewed and edited the manuscript to finalize it for publication.

620 *Competing interests.* No competing interests are present.

Acknowledgements. This work was funded by the Deutsche Forschungsgemeinschaft (DFG – German Research Foundation) under the Research Grants Programme - Individual Proposal with title "Precipitation life cycle in trade wind cumuli", project number 437320342, <https://gepris.dfg.de/gepris/projekt/437320342>.

We gratefully acknowledge the support by the SFB/TR 172 "Arctic Amplification: Climate Relevant Atmospheric and Surface Processes, and Feedback Mechanisms (AC)³" funded by the DFG (Deutsche Forschungsgemeinschaft).

This article is partially based upon work from COST Action PROBE, supported by COST (European Cooperation in Science and Technology), www.cost.eu.

We want to thank Rainer Haseneder-Lind, the ARM team, and Steven M. Bormet, for their fantastic support and collaboration in the testing phase of the installment of the stabilization platform on the ship in Emden (DE), for the help and the patience provided after the campaign, for the correction of the data and the delays in the upload on the ARM database. We also thank Jun. Prof. Heike Kalesse-Los and Johannes Rötthenbacher for deploying the MRR-PRO on the MS Merian and for the fruitful discussion on in the development phase of the correction algorithm. We want to thank Annika Daehne for the administrative support she provided across the different phases of the campaign.

We also would like to acknowledge the ship crew for the brilliant support offered in the installation of the equipment onboard MS Merian and for facing all the technical issues encountered during the campaign. We thank Daniel Klocke, for running ICON simulations that were used for correcting the radar data from ship motions. Finally, we thank Markus Ritschel for the fruitful discussions onboard MS Merian on how to implement the correction for ship motions, and the scientific crew onboard MS Merian for the collaborations developed onboard, with a special thanks to Prof. Eberhard Bodenschatz for finally fixing the stabilization platform. We thank Juan Antonio Bravo Aranda and Lukas Pfitzenmaier for the work done for developing the post-processing radar Matlab software tool that was used in this work.

References

- 640 Acquistapace, C.: Investigation of drizzle onset in liquid clouds using ground based active and passive remote sensing instruments, text.thesis.doctoral, University of Cologne, Cologne, Germany, <http://kups.ub.uni-koeln.de/7932/>, 2017.
- Acquistapace, C., Löhnert, U., Maahn, M., and Kollias, P.: A new criterion to improve operational drizzle detection with ground-based remote sensing, *Journal of Atmospheric and Oceanic Technology*, <https://doi.org/10.1175/JTECH-D-18-0158.1>, <https://journals.ametsoc.org/doi/abs/10.1175/JTECH-D-18-0158.1>, 2019.
- 645 Acquistapace, C., Garcia-Benadi, A., Schween, J. H., Haseneder-Lind, R., Roettenbacher, J., Klocke, D., Kalesse-Los, H., Bormet, S., and Coulter, R. L.: MRR-PRO radar dataset, <https://doi.org/10.25326/233>, <https://doi.org/10.25326/233>, 2021a.
- Acquistapace, C., Risse, N., Schween, J. H., Haseneder-Lind, R., Roettenbacher, J., Klocke, D., Kalesse-Los, H., Bormet, S., Coulter, R. L., Myagkov, A., and T., R.: W band radar dataset, <https://doi.org/10.25326/156>, <https://doi.org/10.25326/156>, 2021b.
- Acquistapace, C., Risse, N., Schween, J. H., Haseneder-Lind, R., Roettenbacher, J., Klocke, D., Kalesse-Los, H., Bormet, S., Coulter, R. L., Myagkov, A., and T., R.: W band radar dataset (V2), <https://doi.org/10.25326/235>, <https://doi.org/10.25326/235>, 2021c.
- 650 Bange, J., Esposito, M., Lenschow, D. H., Brown, P. R. A., Dreiling, V., Giez, A., Mahrt, L., Malinowski, S. P., Rodi, A. R., Shaw, R. A., Siebert, H., Smit, H., and Zöger, M.: Measurement of Aircraft State and Thermodynamic and Dynamic Variables, chap. 2, pp. 7–75, John Wiley Sons, Ltd, <https://doi.org/https://doi.org/10.1002/9783527653218.ch2>, <https://onlinelibrary.wiley.com/doi/abs/10.1002/9783527653218.ch2>, 2013.
- 655 Bony, S. and Dufresne, J.-L.: Marine boundary layer clouds at the heart of tropical cloud feedback uncertainties in climate models, *Geophysical Research Letters*, 32, <https://doi.org/10.1029/2005GL023851>, <https://agupubs.onlinelibrary.wiley.com/doi/abs/10.1029/2005GL023851>, 2005.
- Bony, S., Stevens, B., Ament, F., Bigorre, S., Chazette, P., Crewell, S., Delanoë, J., Emanuel, K., Farrell, D., Flamant, C., Gross, S., Hirsch, L., Karstensen, J., Mayer, B., Nuijens, L., Ruppert, J. H., Sandu, I., Siebesma, P., Speich, S., Szczap, F., Totems, J., Vogel, R., Wendisch, M., and Wirth, M.: EUREC4A: A Field Campaign to Elucidate the Couplings Between Clouds, Convection and Circulation, *Surveys in Geophysics*, 38, 1529–1568, <https://doi.org/10.1007/s10712-017-9428-0>, <https://doi.org/10.1007/s10712-017-9428-0>, 2017.
- 660 Bony, S., Schulz, H., Vial, J., and Stevens, B.: Sugar, Gravel, Fish, and Flowers: Dependence of Mesoscale Patterns of Trade-Wind Clouds on Environmental Conditions, *Geophysical Research Letters*, 47, e2019GL085988, <https://doi.org/https://doi.org/10.1029/2019GL085988>, <https://agupubs.onlinelibrary.wiley.com/doi/abs/10.1029/2019GL085988>, 2020.
- 665 Bossler, P., Bock, O., Flamant, C., Bony, S., and Speich, S.: Integrated water vapour content retrievals from ship-borne GNSS receivers during EUREC⁴A, *Earth System Science Data*, 13, 1499–1517, <https://doi.org/10.5194/essd-13-1499-2021>, <https://essd.copernicus.org/articles/13/1499/2021/>, publisher: Copernicus GmbH, 2021.
- Bretherton, C. S., Wood, R., George, R. C., Leon, D., Allen, G., and Zheng, X.: Southeast Pacific stratocumulus clouds, precipitation and boundary layer structure sampled along 20° S during VOCALS-REx, *Atmospheric Chemistry and Physics*, 10, 10639–10654, <https://doi.org/10.5194/acp-10-10639-2010>, <https://acp.copernicus.org/articles/10/10639/2010/>, publisher: Copernicus GmbH, 2010.
- 670 Coulter, R. L. and Martin, T. J.: Report on the Second ARM Mobile Facility (AMF2) Roll, Pitch, and Heave (RPH) Stabilization Platform: Design and Evaluation, Tech. Rep. DOE/SC-ARM-TR-166, DOE ARM Climate Research Facility, Pacific Northwest National Laboratory, Richland, WA, <https://doi.org/10.2172/1253916>, <https://www.osti.gov/biblio/1253916>, 2016.
- Dee, D. P., Uppala, S. M., Simmons, A. J., Berrisford, P., Poli, P., Kobayashi, S., Andrae, U., Balmaseda, M. A., Balsamo, G., Bauer, P., Bechtold, P., Beljaars, A. C. M., Berg, L. v. d., Bidlot, J., Bormann, N., Delsol, C., Dragani, R., Fuentes, M., Geer, A. J., Haim-

- berger, L., Healy, S. B., Hersbach, H., Hólm, E. V., Isaksen, L., Kållberg, P., Köhler, M., Matricardi, M., McNally, A. P., Monge-Sanz, B. M., Morcrette, J.-J., Park, B.-K., Peubey, C., Rosnay, P. d., Tavolato, C., Thépaut, J.-N., and Vitart, F.: The ERA-Interim reanalysis: configuration and performance of the data assimilation system, *Quarterly Journal of the Royal Meteorological Society*, 137, 553–597, <https://doi.org/https://doi.org/10.1002/qj.828>, <https://rmets.onlinelibrary.wiley.com/doi/abs/10.1002/qj.828>, 2011.
- 680 Frenger, I., Gruber, N., Knutti, R., and Münnich, M.: Imprint of Southern Ocean eddies on winds, clouds and rainfall, *Nature Geoscience*, 6, 608–612, <https://doi.org/10.1038/ngeo1863>, <https://www.nature.com/articles/ngeo1863>, bandiera_abtest: a Cg_type: Nature Research Journals Number: 8 Primary_atype: Research Publisher: Nature Publishing Group Subject_term: Marine biology Subject_term_id: marine-biology, 2013.
- Garcia-Benadi, A., Gonzalez, S., Udina, M., Codina, B., and Georgis, J.-F.: Precipitation Type Classification of Micro Rain Radar Data Using an Improved Doppler Spectral Processing Methodology, *Remote Sensing*, 12, 4113, <https://doi.org/10.3390/rs12244113>, <https://www.mdpi.com/2072-4292/12/24/4113>, 2020.
- Garcia-Benadi, A., Bech, J., Gonzalez, S., Udina, M., and Codina, B.: A New Methodology to Characterise the Radar Bright Band Using Doppler Spectral Moments from Vertically Pointing Radar Observations, *Remote Sensing*, 13, <https://doi.org/10.3390/rs13214323>, <https://www.mdpi.com/2072-4292/13/21/4323>, 2021.
- 690 Gramazio, C. C., Laidlaw, D. H., and Schloss, K. B.: Colorgical: Creating discriminable and preferable color palettes for information visualization, *IEEE Transactions on Visualization and Computer Graphics*, 23, 521–530, <https://doi.org/10.1109/TVCG.2016.2598918>, conference Name: IEEE Transactions on Visualization and Computer Graphics, 2017.
- Hildebrand, P. H. and Sekhon, R. S.: Objective Determination of the Noise Level in Doppler Spectra, *Journal of Applied Meteorology*, 13, 808–811, [https://doi.org/10.1175/1520-0450\(1974\)013<0808:ODOTNL>2.0.CO;2](https://doi.org/10.1175/1520-0450(1974)013<0808:ODOTNL>2.0.CO;2), 1974.
- 695 Hou, A. Y., Kakar, R. K., Neeck, S., Azarbarzin, A. A., Kummerow, C. D., Kojima, M., Oki, R., Nakamura, K., and Iguchi, T.: The Global Precipitation Measurement Mission, *Bulletin of the American Meteorological Society*, 95, 701–722, <https://doi.org/10.1175/BAMS-D-13-00164.1>, <https://journals.ametsoc.org/view/journals/bams/95/5/bams-d-13-00164.1.xml>, publisher: American Meteorological Society Section: Bulletin of the American Meteorological Society, 2014.
- Illingworth, A. J., Barker, H. W., Beljaars, A., Ceccaldi, M., Chepfer, H., Clerbaux, N., Cole, J., Delanoë, J., Domenech, C., Donovan, D. P., Fukuda, S., Hidakata, M., Hogan, R. J., Huenerbein, A., Kollias, P., Kubota, T., Nakajima, T., Nakajima, T. Y., Nishizawa, T., Ohno, Y., Okamoto, H., Oki, R., Sato, K., Satoh, M., Shephard, M. W., Velázquez-Blázquez, A., Wandinger, U., Wehr, T., and Zadelhoff, G.-J. v.: The EarthCARE Satellite: The Next Step Forward in Global Measurements of Clouds, Aerosols, Precipitation, and Radiation, *Bulletin of the American Meteorological Society*, 96, 1311–1332, <https://doi.org/10.1175/BAMS-D-12-00227.1>, <https://journals.ametsoc.org/view/journals/bams/96/8/bams-d-12-00227.1.xml>, publisher: American Meteorological Society Section: Bulletin of the American Meteorological Society, 2015.
- 705 Jacob, M., Ament, F., Gutleben, M., Konow, H., Mech, M., Wirth, M., and Crewell, S.: Investigating the liquid water path over the tropical Atlantic with synergistic airborne measurements, *Atmospheric Measurement Techniques*, 12, 3237–3254, <https://doi.org/10.5194/amt-12-3237-2019>, <https://amt.copernicus.org/articles/12/3237/2019/>, publisher: Copernicus GmbH, 2019.
- Kollias, P., Clothiaux, E. E., Miller, M. A., Albrecht, B. A., Stephens, G. L., and Ackerman, T. P.: Millimeter-Wavelength Radars: New Frontier in Atmospheric Cloud and Precipitation Research, *Bulletin of the American Meteorological Society*, 88, 1608–1624, <https://doi.org/10.1175/BAMS-88-10-1608>, <https://journals.ametsoc.org/doi/abs/10.1175/BAMS-88-10-1608>, 2007.
- 710

- Kollias, P., Rémillard, J., Luke, E., and Szyrmer, W.: Cloud radar Doppler spectra in drizzling stratiform clouds: 1. Forward modeling and remote sensing applications, *Journal of Geophysical Research: Atmospheres*, 116, D13 201, <https://doi.org/10.1029/2010JD015237>, <http://onlinelibrary.wiley.com/doi/10.1029/2010JD015237/abstract>, 2011a.
- 715 Kollias, P., Szyrmer, W., Rémillard, J., and Luke, E.: Cloud radar Doppler spectra in drizzling stratiform clouds: 2. Observations and microphysical modeling of drizzle evolution, *Journal of Geophysical Research: Atmospheres*, 116, D13 203, <https://doi.org/10.1029/2010JD015238>, <http://onlinelibrary.wiley.com/doi/10.1029/2010JD015238/abstract>, 2011b.
- Küchler, N., Kneifel, S., Löhnert, U., Kollias, P., Czekala, H., and Rose, T.: A W-Band Radar–Radiometer System for Accurate and Continuous Monitoring of Clouds and Precipitation, *Journal of Atmospheric and Oceanic Technology*, 34, 2375–
720 2392, <https://doi.org/10.1175/JTECH-D-17-0019.1>, <https://journals.ametsoc.org/view/journals/atot/34/11/jtech-d-17-0019.1.xml>, publisher: American Meteorological Society Section: *Journal of Atmospheric and Oceanic Technology*, 2017.
- Lamer, K., Kollias, P., and Nuijens, L.: Observations of the variability of shallow trade wind cumulus cloudiness and mass flux, *Journal of Geophysical Research: Atmospheres*, 120, 6161–6178, <https://doi.org/https://doi.org/10.1002/2014JD022950>, <https://agupubs.onlinelibrary.wiley.com/doi/abs/10.1002/2014JD022950>, <https://agupubs.onlinelibrary.wiley.com/doi/pdf/10.1002/2014JD022950>, 2015.
- 725 Lamer, K., Kollias, P., Battaglia, A., and Preval, S.: Mind the gap – Part 1: Accurately locating warm marine boundary layer clouds and precipitation using spaceborne radars, *Atmospheric Measurement Techniques*, 13, 2363–2379, <https://doi.org/10.5194/amt-13-2363-2020>, <https://amt.copernicus.org/articles/13/2363/2020/>, publisher: Copernicus GmbH, 2020.
- Laxenaire, R., Speich, S., Blanke, B., Chaigneau, A., Pegliasco, C., and Stegner, A.: Anticyclonic Eddies Connecting
730 the Western Boundaries of Indian and Atlantic Oceans, *Journal of Geophysical Research: Oceans*, 123, 7651–7677, <https://doi.org/https://doi.org/10.1029/2018JC014270>, <https://agupubs.onlinelibrary.wiley.com/doi/abs/10.1029/2018JC014270>, 2018.
- Leon, D. C., Wang, Z., and Liu, D.: Climatology of drizzle in marine boundary layer clouds based on 1 year of data from CloudSat and Cloud-Aerosol Lidar and Infrared Pathfinder Satellite Observations (CALIPSO), *Journal of Geophysical Research: Atmospheres*, 113, publisher: Wiley Online Library, 2008.
- 735 Liebe, H. J., Hufford, G. A., and Manabe, T.: A model for the complex permittivity of water at frequencies below 1 THz, *International Journal of Infrared and Millimeter Waves*, 12, 659–675, <https://doi.org/10.1007/BF01008897>, <https://doi.org/10.1007/BF01008897>, 1991.
- Liebe, H. J., Hufford, G. A., and Cotton, M. G.: Propagation modeling of moist air and suspended water/ice particles at frequencies below 1000 GHz, *Environmental Science, Chemistry*, conference Name: AGARD, *Atmospheric Propagation Effects Through Natural and Man-Made Obscurants for Visible to MM-Wave Radiation* 11 p (SEE N94-30495 08-32), 1993.
- 740 Luke, E. P. and Kollias, P.: Separating Cloud and Drizzle Radar Moments during Precipitation Onset Using Doppler Spectra, *Journal of Atmospheric and Oceanic Technology*, 30, 1656–1671, <https://doi.org/10.1175/JTECH-D-11-00195.1>, <http://journals.ametsoc.org/doi/abs/10.1175/JTECH-D-11-00195.1>, 2013.
- Löhnert, U. and Crewell, S.: Accuracy of cloud liquid water path from ground-based microwave radiometry 1. Dependency on cloud model statistics, *Radio Science*, 38, <https://doi.org/https://doi.org/10.1029/2002RS002654>, <https://agupubs.onlinelibrary.wiley.com/doi/abs/10.1029/2002RS002654>, 2003.
- 745 Peters, G., Fischer, B., and Andersson, T.: Rain observations with a vertically looking Micro Rain Radar (MRR)., *Boreal Environ. Res.*, 7, 353–362, 2002.

- Platnick, S., King, M., Ackerman, S., Menzel, W., Baum, B., Riedi, J., and Frey, R.: The MODIS cloud products: algorithms and examples from Terra, *IEEE Transactions on Geoscience and Remote Sensing*, 41, 459–473, <https://doi.org/10.1109/TGRS.2002.808301>, conference
750 Name: *IEEE Transactions on Geoscience and Remote Sensing*, 2003.
- Rosenkranz, P. W.: Water vapor microwave continuum absorption: A comparison of measurements and models, *Radio Science*, 33, 919–928, <https://doi.org/https://doi.org/10.1029/98RS01182>, <https://agupubs.onlinelibrary.wiley.com/doi/abs/10.1029/98RS01182>, 1998.
- Rosenkranz, P. W.: Correction to “Water vapor microwave continuum absorption: A comparison of measurements and models”, *Radio
755 Science*, 34, 1025–1025, <https://doi.org/https://doi.org/10.1029/1999RS900020>, <https://agupubs.onlinelibrary.wiley.com/doi/abs/10.1029/1999RS900020>, 1999.
- Schnitt, S., Orlandi, E., Mech, M., Ehrlich, A., and Crewell, S.: Characterization of Water Vapor and Clouds During the Next-Generation Aircraft Remote Sensing for Validation (NARVAL) South Studies, *IEEE Journal of Selected Topics in Applied Earth Observations and Remote Sensing*, 10, 3114–3124, <https://doi.org/10.1109/JSTARS.2017.2687943>, 2017.
- Stephan, C. C., Schnitt, S., Schulz, H., Bellenger, H., de Szoeko, S. P., Acquistapace, C., Baier, K., Dauhut, T., Laxenaire, R., Morfa-Avalos,
760 Y., Person, R., Quiñones Meléndez, E., Bagheri, G., Böck, T., Daley, A., Güttler, J., Helfer, K. C., Los, S. A., Neuberger, A., Röttenbacher, J., Raeke, A., Ringel, M., Ritschel, M., Sadoulet, P., Schirmacher, I., Stolla, M. K., Wright, E., Charpentier, B., Doerenbecher, A., Wilson, R., Jansen, F., Kinne, S., Reverdin, G., Speich, S., Bony, S., and Stevens, B.: Ship- and island-based atmospheric soundings from the 2020 EUREC⁴A field campaign, *Earth System Science Data*, 13, 491–514, <https://doi.org/10.5194/essd-13-491-2021>, <https://essd.copernicus.org/articles/13/491/2021/>, publisher: Copernicus GmbH, 2021.
- 765 Stevens, B., Bony, S., Farrell, D., Ament, F., Blyth, A., Fairall, C., Karstensen, J., Quinn, P. K., Speich, S., Acquistapace, C., Aemisegger, F., Albright, A. L., Bellenger, H., Bodenschatz, E., Caesar, K.-A., Chewitt-Lucas, R., de Boer, G., Delanö, J., Denby, L., Ewald, F., Fildier, B., Forde, M., George, G., Gross, S., Hagen, M., Hausold, A., Heywood, K. J., Hirsch, L., Jacob, M., Jansen, F., Kinne, S., Klocke, D., Kölling, T., Konow, H., Lathon, M., Mohr, W., Naumann, A. K., Nuijens, L., Olivier, L., Pincus, R., Pöhlker, M., Reverdin, G., Roberts, G., Schnitt, S., Schulz, H., Siebesma, A. P., Stephan, C. C., Sullivan, P., Touzé-Peiffer, L., Vial, J., Vogel, R., Zuidema, P., Alexander,
770 N., Alves, L., Arixí, S., Asmath, H., Bagheri, G., Baier, K., Bailey, A., Baranowski, D., Baron, A., Barrau, S., Barrett, P. A., Batier, F., Behrendt, A., Bendinger, A., Beucher, F., Bigorre, S., Blades, E., Blossey, P., Bock, O., Böing, S., Bosser, P., Bourras, D., Bouruet-Aubertot, P., Bower, K., Branellec, P., Branger, H., Brennek, M., Brewer, A., Brilouet, P.-E., Brüggemann, B., Buehler, S. A., Burke, E., Burton, R., Calmer, R., Canonici, J.-C., Carton, X., Cato Jr., G., Charles, J. A., Chazette, P., Chen, Y., Chilinski, M. T., Choulaton, T., Chuang, P., Clarke, S., Coe, H., Cornet, C., Coutris, P., Couvreur, F., Crewell, S., Cronin, T., Cui, Z., Cuypers, Y., Daley, A., Damerell,
775 G. M., Dauhut, T., Deneke, H., Desbios, J.-P., Dörner, S., Donner, S., Douet, V., Drushka, K., Dütsch, M., Ehrlich, A., Emanuel, K., Emmanouilidis, A., Etienne, J.-C., Etienne-Leblanc, S., Faure, G., Feingold, G., Ferrero, L., Fix, A., Flamant, C., Flatau, P. J., Foltz, G. R., Forster, L., Furtuna, I., Gadian, A., Galewsky, J., Gallagher, M., Gallimore, P., Gaston, C., Gentemann, C., Geyskens, N., Giez, A., Gollop, J., Gouirand, I., Gourbeyre, C., de Graaf, D., de Groot, G. E., Grosz, R., Güttler, J., Gutleben, M., Hall, K., Harris, G., Helfer, K. C., Henze, D., Herbert, C., Holanda, B., Ibanez-Landeta, A., Intrieri, J., Iyer, S., Julien, F., Kalesse, H., Kazil, J., Kellman, A., Kidane,
780 A. T., Kirchner, U., Klingebiel, M., Körner, M., Kremper, L. A., Kretzschmar, J., Krüger, O., Kumala, W., Kurz, A., L'Hégaret, P., Labaste, M., Lachlan-Cope, T., Laing, A., Landschützer, P., Lang, T., Lange, D., Lange, I., Laplace, C., Lavik, G., Laxenaire, R., Le Bihan, C., Leandro, M., Lefevre, N., Lena, M., Lenschow, D., Li, Q., Lloyd, G., Los, S., Losi, N., Lovell, O., Luneau, C., Makuch, P., Malinowski, S., Manta, G., Marinou, E., Marsden, N., Masson, S., Maury, N., Mayer, B., Mayers-Als, M., Mazel, C., McGeary, W., McWilliams, J. C., Mech, M., Mehlmann, M., Meroni, A. N., Mieslinger, T., Minikin, A., Minnett, P., Möller, G., Morfa Avalos, Y., Muller, C., Musat, I.,
785 Napoli, A., Neuberger, A., Noisel, C., Noone, D., Nordsiek, F., Nowak, J. L., Oswald, L., Parker, D. J., Peck, C., Person, R., Philippi, M.,

- Plueddemann, A., Pöhlker, C., Pörtge, V., Pöschl, U., Pologne, L., Posyniak, M., Prange, M., Quiñones Meléndez, E., Radtke, J., Ramage, K., Reimann, J., Renault, L., Reus, K., Reyes, A., Ribbe, J., Ringel, M., Ritschel, M., Rocha, C. B., Rochetin, N., Röttenbacher, J., Rollo, C., Royer, H., Sadoulet, P., Saffin, L., Sandiford, S., Sandu, I., Schäfer, M., Schemann, V., Schirmacher, I., Schlenczek, O., Schmidt, J., Schröder, M., Schwarzenboeck, A., Sealy, A., Senff, C. J., Serikov, I., Shohan, S., Siddle, E., Smirnov, A., Späth, F., Spooner, B., Stolla, M. K., Szkółka, W., de Szoeko, S. P., Tarot, S., Tetoni, E., Thompson, E., Thomson, J., Tomassini, L., Totems, J., Ubele, A. A., Villiger, L., von Arx, J., Wagner, T., Walther, A., Webber, B., Wendisch, M., Whitehall, S., Wiltshire, A., Wing, A. A., Wirth, M., Wiskandt, J., Wolf, K., Worbes, L., Wright, E., Wulfmeyer, V., Young, S., Zhang, C., Zhang, D., Ziemann, F., Zinner, T., and Zöger, M.: EUREC⁴A, Earth System Science Data Discussions, pp. 1–78, <https://doi.org/10.5194/essd-2021-18>, <https://essd.copernicus.org/preprints/essd-2021-18/>, publisher: Copernicus GmbH, 2021.
- 790
- 795 Ulaby, F., Moore, R., and Fung, A.: Microwave remote sensing: Active and passive. Volume 1 - Microwave remote sensing fundamentals and radiometry, Artech House, <https://ntrs.nasa.gov/citations/19820039342>, 1981.
- Zeller, S. and Rogers, D.: Visualizing Science: How Color Determines What We See, <https://eos.org/features/visualizing-science-how-color-determines-what-we-see>, 2020.
- 800 Zhou, X., Kollias, P., and Lewis, E. R.: Clouds, Precipitation, and Marine Boundary Layer Structure during the MAGIC Field Campaign, *Journal of Climate*, 28, 2420–2442, <https://doi.org/10.1175/JCLI-D-14-00320.1>, <https://journals.ametsoc.org/view/journals/clim/28/6/jcli-d-14-00320.1.xml>, publisher: American Meteorological Society Section: *Journal of Climate*, 2015.

Table 3. Daily mean values of the main surface variables observed on the MS Merian during the EUREC⁴A campaign: T2m is the air temperature 2m above the radar base, which is approximately 20 m above sea level, RR is the rain rate. The liquid water path (LWP) is derived from the collocated 89 GHz channel microwave radiometer and RH and P are the relative humidity and air pressure from a weather station positioned next to the radar equipment.

DAY	T2m [$^{\circ}\text{C}$]	RR [mmh^{-1}]	LWP [gm^{-2}]	RH [%]	P [hPa]
19.01.2020	26.35	0.0	1.	63.6	1013.9
20.01.2020	25.95	0.57	30.	72.4	1013.3
21.01.2020	26.85	1.0	71.	67.2	1011.7
22.01.2020	27.25	1.42	0.	63.2	1010.3
23.01.2020	26.85	0.99	12.	69.2	1009.7
24.01.2020	26.15	0.57	318.	76.2	1010.4
25.01.2020	26.85	0.67	13.	67.5	1011.9
26.01.2020	26.65	0.0	23.	67.4	1012.2
27.01.2020	26.95	1.37	391.	75.2	1012.0
28.01.2020	27.25	0.0	50.	74.9	1010.8
29.01.2020	27.15	0.32	26.	72.4	1010.9
30.01.2020	27.55	0.0	20.	71.5	1011.7
31.01.2020	27.35	0.0	8.	70.0	1012.7
01.02.2020	27.45	0.31	13.	64.8	1013.0
02.02.2020	27.45	0.49	6.	62.3	1012.0
03.02.2020	27.05	0.0	3.	68.2	1013.3
04.02.2020	27.25	0.0	8.	69.2	1013.1
05.02.2020	27.05	0.45	10.	68.3	1014.1
06.02.2020	27.15	0.0	11.	65.7	1013.9
07.02.2020	26.75	1.77	31.	63.7	1013.9
08.02.2020	26.55	7.43	35.	65.8	1013.6
09.02.2020	26.85	1.38	4.	66.3	1015.3
10.02.2020	26.65	0.80	106.	67.3	1015.1
11.02.2020	26.55	0.30	54.	68.7	1014.6
12.02.2020	26.35	0.43	85.	70.3	1014.1
13.02.2020	26.55	0.70	51.	68.5	1012.7
14.02.2020	27.35	3.24	53.	67.3	1012.9
15.02.2020	26.85	0.89	22.	68.0	1012.1
16.02.2020	26.75	1.06	47.	70.2	1011.3
17.02.2020	27.05	0.33	15.	68.6	1011.9
18.02.2020	26.75	4.22	312.	71.4	1013.2
19.02.2020	26.05	0.62	319.	74.1	1013.1

Table A1. Information about the radiosonde stations (data taken from <https://ruc.noaa.gov/raobs/intl/>) and the ERA-Interim data point used for the retrieval of LWP using neural networks.

Data type	Station name	Station number	Station lat/lon
radiosonde	BB-GRANTLEY-ADAMS-INTL	00078954	13.040 / -59.290 (z = 56.0 m)
radiosonde	MF-LE-RAIZET-GUADELOUP	00078897	16.160 / -61.310 (z = 8.0 m)
radiosonde	TD-PIARCO-INTL-AIRPORT	00078970	10.370 / -61.210 (z = 15.0 m)
ERA-Interim	BB-ERA-Barbados	30401103	12.750 / -59.250 (z = 12.5 m)